__Original Research Article__

Effect of different annealing temperatures on structural, optical, morphological and electrical properties of Cu - ZnO thin films prepared using sol—gel spin Coating techniques.

ABSTRACT

In this study, Cu - doped ZnO thin films were prepared at different annealing temperatures from Copper acetate precursor by sol-gel spin coating method for Photocatalytic Applications. The films were characterized by X-ray diffractometer (XRD), scanning electron microscopy (SEM), and Fourier transform infrared spectroscopy (FTIR). The obtained powders were annealed under air in the range of $T_c = 250^0 - 550^0 \, C,$ for Cu – ZnO. The surface morphological, structural, electrical and optical properties of the as-deposited ZnO films have been investigated as a function of Cu-doping level. The thickness of the films was estimated by Fizeau fringes interference method which varied from 195 to 198 nm. The X-ray diffraction analysis indicated that the wurtzite structure was maintained for all samples and copper was successfully doped into ZnO at low T_C. However, the formation of monoclinic CuO was observed at higher T_C. For Cu – ZnO, the crystallite size increased with the annealing temperature from 15.86 to 24.24 nm. The isotherms obtained were type IV with a hysteresis type H 3, confirming the mesoporous behavior of the catalysts. The surface area was in the range of 35.1 to 8.66 m^2/g. All the prepared catalysts mainly showed two emission regions: a sharp peak in the ultraviolet region and another broad peak in the visible region. The photocatalytic activity was achieved by the degradation of 300 mg/L malachite green (MG) aqueous solution under UV irradiation. The findings showed that the increased annealing of different concentration of Cu doped ZnO with CuO on the surface resulted in highly improved photocatalytic activity. Various optical constants such as absorbance, transmittance of the films have been studied. The values of transmittance are high in the visible and IR region and it is minimum in the UV region. Absorbance decreases with higher percentage of Cu concentration. The band gap of the films varied 3.21 to 3.05 eV. The resistivity gradually decreases with the increase of temperature, which indicates the semiconducting nature of the materials. Resistivity also increases with the increasing doping concentration. The conductivity decreases with the increasing of Cu concentration.

Keyword: Zinc Oxide; Sol – gel; Malachite Green; Annealing Temperature; Copper; Photocatalytic Activity; Resistivity; Conductivity.

46

47   **1. Introduction**

48

49   Nanotechnology can be better demonstrated by the technology of design and applications of
50   nanomaterials. Nanoscale oxides of transition metals are of most significance for several
51   applications in optoelectronics [1]. The most emerging technology in today's world is
52   Transparent Electronics through which wide bandgap semiconductors are applied in
53   applications of optoelectronic devices [2] and potent exciting binding energy of 60 meV [3].
54   Also, Nanoscale Oxides has other important application such as solar cell, gas sensor, Li-ion
55   batteries, supercapacitors [4]. The important advantages of ZnO include its ability to absorb
56   large quantity of visible light than TiO_2, environmental sustainability, its low cost and high
57   catalytic efficiency. For this reason, ZnO is suitable and more effective in the photocatalytic
58   degradation of some dyes. ZnO crystallizes in a hexagonal wurtzite structure with the lattice
59   parameters of (c = 5.205 Å, a = 3.249 Å) [5]. Doping ZnO with a transition metal such as Cu
60   [6] has been verified as an effective method to adjust its functionality including electrical and
61   optical properties Cu-doped ZnO has shown significantly improved properties such as
62   electrical, magnetic, photocatalytic performance and gas sensing properties. In practice,
63   ZnO-based thin films can be grown by diverse growth techniques including radio frequency
64   magnetron sputtering (RFMS), pulsed laser deposition (PLD), laser molecular beam epitaxy
65   (P-MBE) [6], spray pyrolysis [7], metal organic chemical vapour deposition (MOCVD) [8],
66   and sol-gel spin coating method [9]. Among these methods, spin coating can provide the
67   ease of chemical composition of doping, which is an advantage over the others. Annealing
68   and doping are important approaches used to improve ZnO as a photocatalyst and are more
69   effective and play important roles in controlling the intrinsic defects of ZnO. Moreover,
70   annealing increases the crystallinity of ZnO, decreases the defect on its surface, and reduces
71   its band gap energy. Radiation handling of polymers is a non-power application and at most
72   consists of cross linking, curing, grafting, and degradation. Ion beam irradiation is a well
73   decided tool for the modification of polymer surfaces, useful for controlled changes of a
74   variety of characteristics, like chemical reactivity, hardness, wear [10 -13]. In the present
75   work, Nanocrystalline thin films are prepared by simple, low-cost sol-gel spin coating
76   technique, and the effect of different annealing temperatures on structural, optical,
77   morphological and electrical properties of the films are investigated for Photocatalytic
78   Applications .The attraction can simply be attributed to the large exciton binding energy of
79   60 meV of ZnO potentially paving the way for efficient room-temperature exciton-based
80   emitters, and sharp transitions facilitating very low threshold semiconductor lasers [14-18].
81   ZnO is a low-cost, ecofriendly, and versatile material to be used to generate emission colors
82   all over the rainbow spectrum. The reason for the color tuning is the band edge emission as
83   well as the different defect related emissions. The defect related emission in ZnO is
84   dependent on the synthesis method, annealing temperature, and several other parameters [19].
85   The nanostructure tailoring of ZnO is dependent on growth conditions and doping
86   concentrations. ZnO nanostructures have attracted a great attention as optical components in
87   nanometer sized electronic devices due to the enhanced quantum confinement effect and high
88   surface to volume ratio [20-22]. Zinc oxide (ZnO) is a technologically useful material due to
89   its wide band gap of 3.37 eV. Furthermore, ZnO has other advantages such as high chemical
90   and physical stability, thermal stability in hydrogen plasma atmosphere, large exciton binding
91   energy of 60 meV [23-25].

92   **2. Experimental section**

93   **2.1Synthesis of ZnO and Cu- doped ZnO nanoparticles**

94   Zinc acetate dihydrate [Zn $(CH_3 COO)_2$ $.2H_2O$], absolute methanol, tartaric acid (CHOH-
95    $COOH)_2$, Copper nitrate trihydrate [$Cu(NO_3)_2$ $.3H_2O$] and malachite green (MG) were
96   purchased from Sigma-Aldrich. All chemicals were utilized without further purification.

97 Double distilled water was used in all solution preparations. Cu – doped ZnO thin films were
98 prepared by sol-gel method using zinc acetate dehydrate $(CH_3 COO)_2 Zn·2H_2O$ and Copper
99 acetate dihydrate $Cu_3[(CH_3 COO)_2·H_2O]$ as starting precursors. The 2-methoxy ethanol
100 $(C_3H_8O_2)$ and diethanal amine (DEA) were selected as the solvent (0.5 M, 100 mL) and sol
101 stabilizer, respectively. The prepared mixture was vigorously stirred at 100 °C for 5 h by
102 magnetic stirrer and cooled to room temperature for 24 h. The precursors prepared at
103 different copper concentration of 2-20 wt.% were spin-coated on borosilicate substrates at
104 room temperature with speed of 3000 rpm for 30 s. After repeating the coating procedure 6-
105 times, all coated films were annealed at various temperatures ranging from 550^0 C for 3 h in
106 ambient air.

107 **2.2 Materials characterization**
108 The morphology of the nanopowder samples was examined using a scanning electron
109 microscope. The samples were previously oven dried and coated with a thin film of gold to
110 provide ZnO powder surface with electrical conduction. The composition and average size of
111 nanoparticles were determined by the powder X-ray diffraction patterns, the samples were
112 recorded by a diffractometer (Bruker D8 – Advance), measurements were performed to
113 identify the structural properties and crystalline behavior of the films using Cu-Kα radiation
114 (λ =0.15406 nm). The accelerating voltage and scanning angle were 40 kV and 20^0 $–75^0$c,
115 respectively. The mode of chemical bonding in the prepared samples was studied by Fourier
116 transform infrared spectroscopy (Model: Nicolet 6700) in the range 4000–400 cm^{-1} with a
117 resolution of 4 cm^{-1}. The surface area and pore sizes of nanoparticles were determined by the
118 Brunauer–Emmett–Teller (BET) method (aims to explain the physical adsorption of gas
119 molecules on a solid surface and serves as the basis for an important analysis technique for
120 the measurement of the specific surface area of materials) using a Micrometrics ASAP 202
121 apparatus (degas temperature: ambient to 200 ^{0}C for20 min with pressure range of 0 to 950
122 mmHg). The optical measurements of the Cu – doped ZnO thin films were carried out at
123 room temperature using spectrophotometer [Labomed – UVS 2800] in the wavelength range
124 of 190 nm to 1100 nm. Room temperature photoluminescence studies were carried out using
125 the (Perkin Elmer LS55 Luminescence).

126 **2.3 Determination of heterogeneous photocatalytic activity**
127 The photoactivity of prepared ZnO and Cu-doped ZnO were examined using (MG) dye as a
128 pollutant and all experiments were carried out in a Pyrex photoreactor under UV irradiation.
129 After achieving adsorption equilibrium in the dark, the solution was illuminated for
130 photocatalytic kinetic study: The samples of the MG solution were taken after different
131 irradiation times and were analysed using UV–visible spectroscopy at a wavelength max=618
132 nm. Using the Beer-Lambert law, the absorption measurement was converted to
133 concentration. The photocatalytic degradation efficiency was calculated using the following
134 equation: [26-27],

135 $$Mg \% = [(C_0 – C_t)/C_0] × 100\% \qquad (1)$$

136 Where C_0 is the [MG] initial concentration, and C_t is the [MG] concentration at time t.

137 **2.4 Film Thickness**
138 The film thicknesses of Cu- ZnO thin films were measured by the Fizeau fringes method in
139 the department of Physics. The thickness of the film "d" can then be determined by the
140 relation:

141 $$d = \frac{\lambda}{2}\frac{a}{b} \qquad (2)$$

142 Where, λ is the wavelength and $\frac{a}{b}$ is the fractional discontinuity. In general, the sodium light
143 is used, for which λ = 5893 Ǻ. In conclusion, it might be mentioned that the Tolansky method
144 of film-thickness measurement is the most widely used and in many respects also the most
145 accurate and satisfactory one. [28-29] The thickness of the films was estimated by Fizeau
146 fringes interference method which varied from 195 to 198 nm.

3. Results and Discussion

3.1 Scanning electron microscopy image (SEM)

The SEM micrographs of ZnO and Cu - ZnO annealed at 550^{0}C was shown in Fig.1. The particles of the obtained powder were spherical in shape with a little agglomeration. Table 1 shows the weight percentages of the elements.
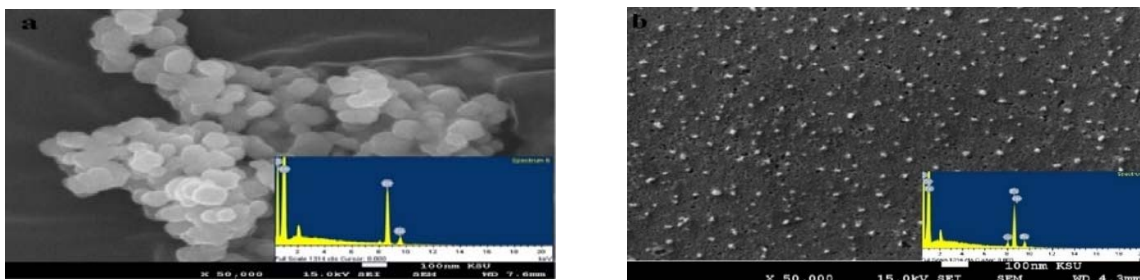

Figure 1: SEM micrographs of ZnO films annealed at (a) 550^{0}c, (b) 20 wt. % Cu doped ZnO film.

It was clearly observed that both films have a smooth surface comprising uniform grain size. As the annealing temperature increases, the crystalline structure and grain size of the film improves. The morphology of the 20 wt. % CZO show mixtures of Nanocrystalline CZO grains and a big number of other granular particles which may be CuO particle due to redundant Cu doping. This characteristic suggested the limitation of Cu doped on ZnO film. The random tendency of grains and the uneven surface may be related to the growth being along different crystal orientation.

Table 1: Weight percentage of the elements obtained from EDX

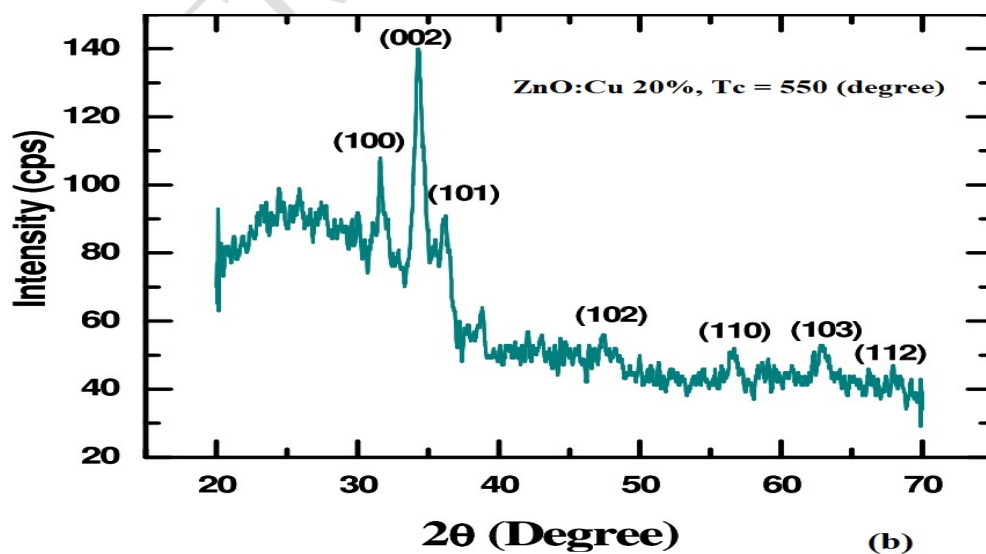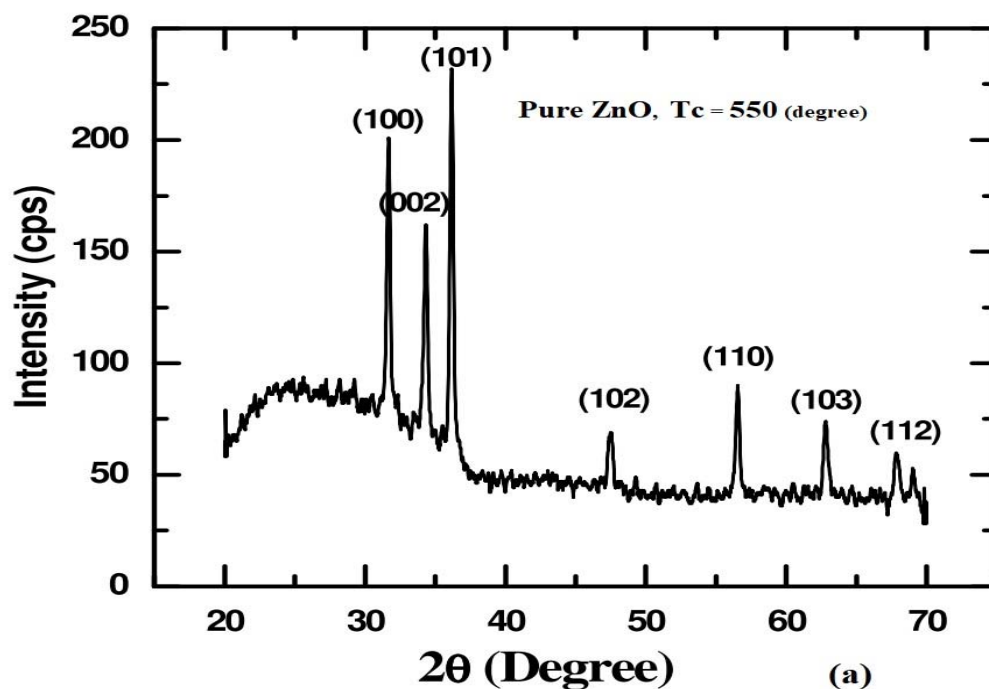| Concentration %	Elements	Wt.%	At%
0	Zn	81.68	60.98
	O	6.68	20.37
5	Zn	46.06	24.58
	Cu	4.74	2.60
	O	15.23	33.20
15	Zn	59.18	37.19
	Cu	10.20	6.60
	O	11.80	30.28
20	Zn	37.69	18.50
	Cu	12.32	5.74
	O	21.20	44.52

3.2 Characterization of the prepared catalysts by X-ray diffraction (XRD)

The structural properties of annealed ZnO and Cu-doped ZnO films on glass substrates are investigated by X-ray diffraction patterns. XRD patterns of ZnO and Cu doped ZnO films at various concentrations are shown in fig 2. The results show broad peaks at positions 31.61^{0}, 34.39^{0}, 36.11^{0}, 47.40^{0}, 56.52^{0}, 62.72^{0}, 66.29^{0}, 67.91^{0} and 69.08^{0} of the spectra. These values are in good agreement with the standard card file (JCPDS 36-1451) for ZnO and can be indexed as the hexagonal wurtzite structure. In addition, the appearance of a very low-intensity diffraction peak at position 38.65^{0}, corresponding to CuO as the monoclinic (base-

173 centered) phase(JCPDS#18-1916) was observed. The appearance of this peak is due to the
174 high quantity of doped Cu and can be detected by XRD. The average crystallite size (D) of
175 the prepared nanomaterial shown in Table 2 was calculated using Scherrer's equation: [30],

176
$$D = \frac{(0.9\,\lambda)}{(\beta\cos\theta)}(3)$$

177 Where, D is the grain diameter, λ is the X-ray wavelength of Cu Kα (0.154 nm), β is the full-
178 width at half maximum (FWHM) and θ is the Bragg angle [31].
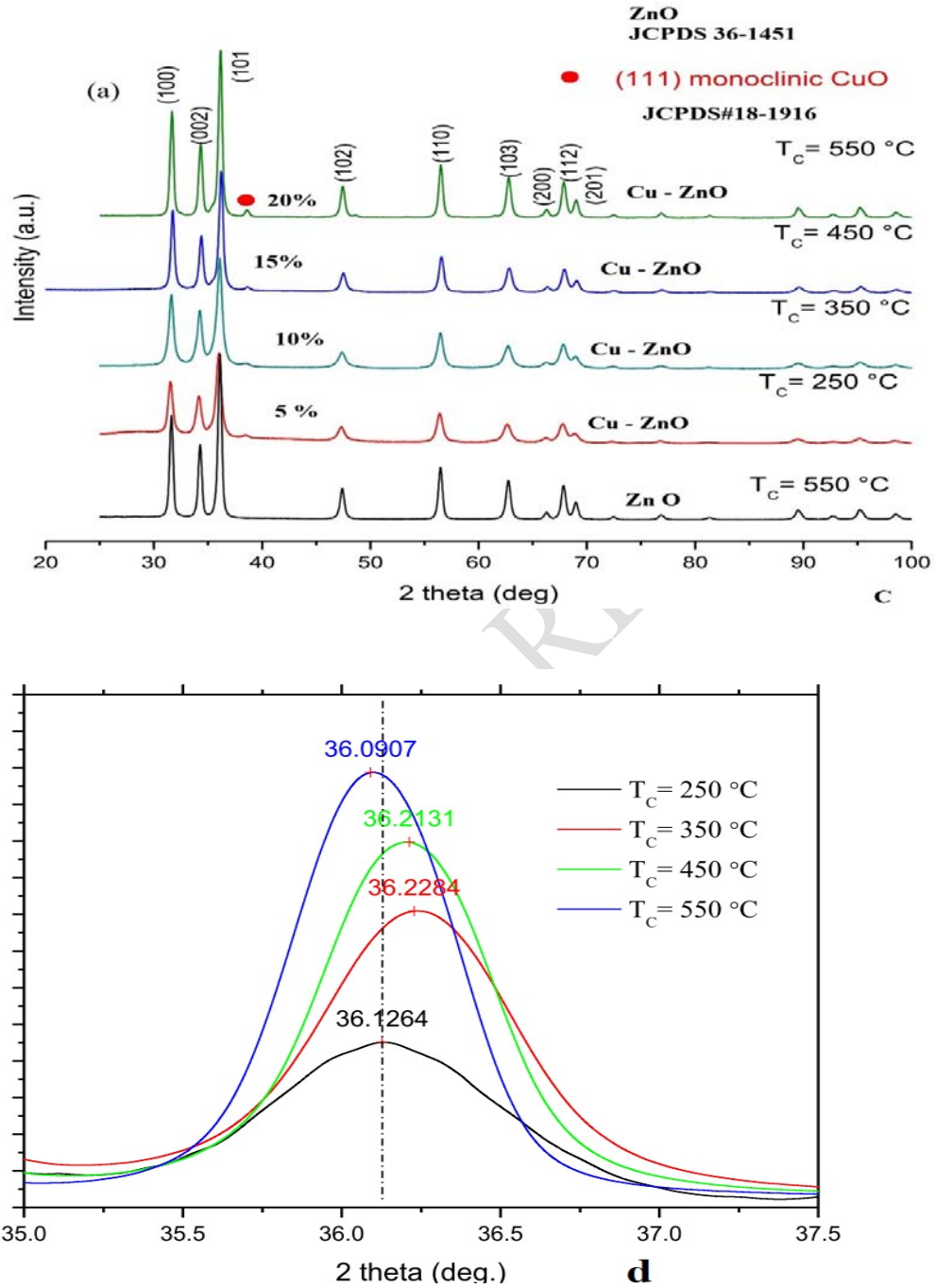179

(a)

180
181
182

(b)

183
184
185

Figure 2: XRD patterns for ZnO and Cu doped ZnO thin films for different Cu concentrations, (a) ZnO (b) ZnO: Cu 20%. (c) XRD patterns of ZnO different Cu concentration thin films with different temperature. (d) XRD principal peak shift due to the effects of the Cu doping and T_C.

The intense peaks in the XRD pattern of all samples clearly show the information of the hexagonal wurtzite phase of ZnO having prominent (002) plane in all samples, which is the most stable phase of ZnO. The shift in the (002) peak for higher Cu concentrations might be the substitution of Zn by Cu in the hexagonal lattice. The effect of Cu doping can be observed

246 at the same annealing temperature ($T_C = 550^0$ C) as shown in Fig. 2. In comparison with
247 ZnO, the introduction of copper ions shifted the diffraction peaks to higher angles by 0.060.
248 Indeed, this change can be attributed to the replacement of Zn ions (ionic radii = 0.60 A) by
249 Cu ions (ionic radii = 0.57 A) or may be due to structural stresses and modification of the
250 lattice parameters of ZnO. This shift value indicated a decrease in the lattice parameters since
251 the value of c parameter decreased by about 0.01 A from undoped ZnO (5.226 A) to Cu-
252 doped ZnO (5.217 A). This decrease confirmed that the substitution of Zn ions by Cu in the
253 ZnO lattice, was facilitated by the similarity of the ionic radii. Sharma et al. [32], in their
254 study on Mn-doped ZnO, reported similar observations.
255 The annealing temperature (T_C) effect was observed on both intensities of XRD peaks and
256 lattice parameters as shown in Fig. 2. Crystallite sizes of the deposited films have been
257 calculated using (002) plane. The values of crystallite sizes are obtained 7.01 nm for ZnO
258 and 3.21 nm, 2.75 nm, 4.82 nm, 3.86 nm and 2.41 nm for ZnO: Cu samples with Cu
259 concentrations 5%, 10 %, 15%, 20% respectively. The grain size values and lattice
260 parameters with different Cu concentrations are given in the following Table 2. Lattice
261 constant slightly vary with doping concentration of Cu but no linear relation with Cu
262 concentration. The shift in the lattice parameter is mainly due to the dopant occupying
263 interstitial positions in the lattice. It is observed that the crystalline size in the doped films
264 does not vary in any regular pattern with Cu dopant concentration, which is attributed to the
265 lattice disorder produced in the films at higher dopant concentration due to difference in the
266 ionic radii of Zn^{2+}amd Cu^{2+} ions and the combination of two different structures, hexagonal
267 and cubic.
268 **Table 2:** Lattice parameters and grain size of undoped and Cu-doped ZnO thin *films*
269

Cu ZnO %	a (Å)	c (Å)	c/a ratio	Grain size (nm)
0	3.2604	5.2244	1.6024	7.01
5	3.2602	5.2277	1.6035	3.21
10	3.2678	5.2293	1.6002	2.75
15	3.2620	5.2210	1.6006	4.82
20	3.2674	5.2272	1.5998	3.86
JCPDS 36-1451	3.249	5.206	1.602	

270

3.3 Fourier transform infrared studies (FTIR)

272 The chemical bonding and formation of wurtzite structure in ZnO and Cu-doped ZnO were
273 confirmed by FTIR measurements at room temperature. The spectra are shown in Fig. 3. The
274 broad absorption band at 3439.39, 1077.74, 3446.53 and 1075.74 cm^{-1} can be attributed to the
275 normal polymeric O-H stretching vibration of H_2O, respectively in ZnO and Cu - ZnO
276 lattices [33]. Other sharp peaks observed at 1621.45 and 1615.60 cm^{-1}can be attributed to H–
277 O–H bending vibration, which in turn can be assigned to the small amount of H_2O in the ZnO
278 and Cu – ZnO nanocrystals [34]. The absorption band observed between2300 and 2400 cm^{-1}
279 are due to the existence of CO_2molecule in the air. The vibration band at446.31 cm^{-1}assigned
280 to the stretching mode of ZnO, shifted to a lower frequency at 438.48 cm^{-1} for Cu - ZnO.

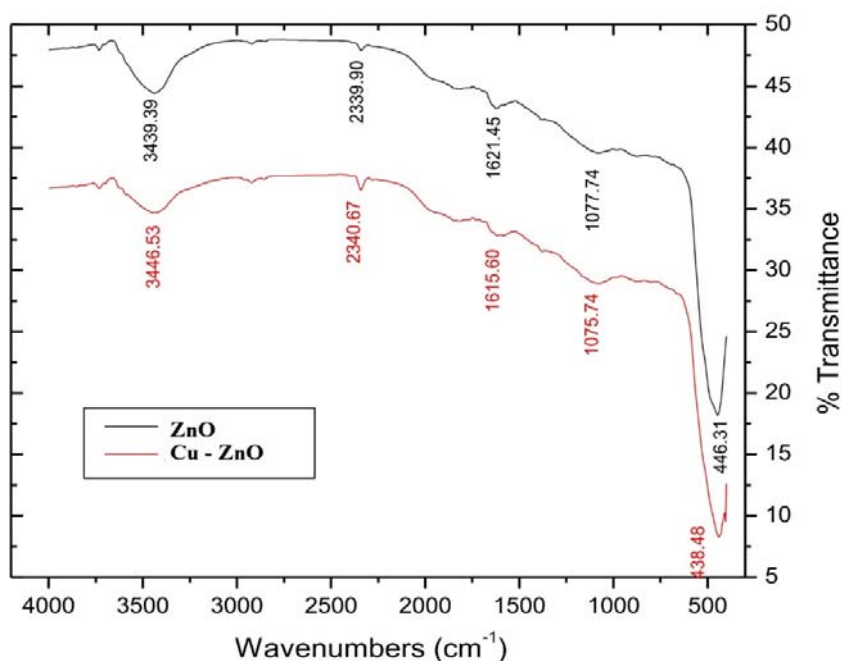281 Hence, it is supposed that Cu-ion can be successfully substituted into the crystal lattice of
282 ZnO [35].
283

Figure 3: FTIR spectra of ZnO and Cu-doped ZnO annealed at 550^0C.

3.4 Surface area analysis (BET)

297 Figure 5 shows the nitrogen adsorption-desorption isotherms and Barett Joyner–Halenda
298 (BJH) pore size distribution for ZnO and Cu-doped annealed at 550^0C. All the isotherms
299 obtained are Type IV and correspond to a capillary condensation, according to the
300 classification of the International Union for Pure and Applied Chemistry (IUPAC). The
301 hysteresis is Type H3, and is characteristic of the mesoporous material with slit-shape pores.
302 Based on the results obtained from Fig. 4, the adsorption of N_2 on ZnO and Cu – ZnO
303 catalysts, slightly increased from a low relative pressure of about 0.02 to 0.8 at higher T_C
304 (450 and 550 ^{0}C) to 0.6 at lower T_C (250 and 350 ^{0}C), and then followed by a sharp rise from
305 0.6 or 0.8 and above due to substantial interparticle porosity [36]. The highest and least
306 volume of absorbed N_2 can be attributed to the catalysts annealed at T_C equal to 250^0 and
307 550^0 C, respectively. All the desorption branches are different from those of adsorption,
308 indicating differences in their pore's texture [37]. Among all the catalysts, Cu -ZnO annealed
309 at $T_C = 250^0$ C showed the highest volume of adsorption and widest desorption branch as
310 shown in Fig. 4. The Barret–Joyner–Halenda (BJH) pore size distribution for all catalysts is
311 shown in Fig. 4. All plots are located in the mesoporous range, which is in good agreement
312 with the Type IV adsorption isotherm. The BJH pore size distribution of ZnO and Cu – ZnO
313 annealed at $T_C = 550$ ^{0}C (Fig. 5) indicates different features of Cu – ZnO annealed at TC =
314 250, 350 and 450 ^{0}C, specifically from the average pore diameter centered at around 70 nm.
315 This shows the result of the modification in pore texture. Based on the obtained results, it can
316 be suggested that the annealing temperature has a clear effect on specific surface area and
317 pore size distribution of the doped catalysts. On the other hand, for the same $T_C = 550$ ^{0}C, the
318 obtained isotherms for ZnO and doped ZnO are very similar, showing almost the same
319 specific surface area. This shows that the effect of doping is less important than the annealing
320 temperature. By increasing the annealing temperature, a remarkable decrease in surface area
321 of ZnO and Cu – ZnO can be observed. This phenomenon could be explained by clogging
322 pores caused by the occurrence of possible aggregation when the annealing temperature

323 increases. This may have the effect of clogging as observed in the diminution of both volume
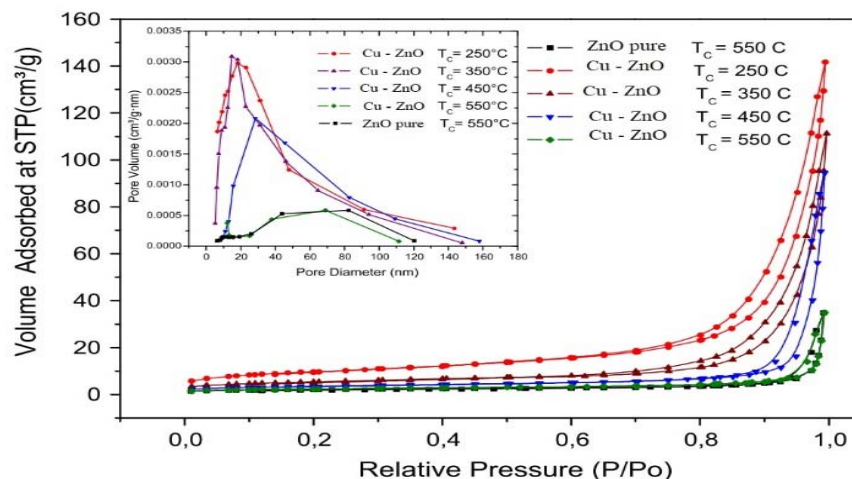324 and average pore size.
325

326

335 **Figure 4**: N₂ adsorption-desorption isotherms and pore size distribution (inset) of ZnO and Cu-doped ZnO
336 annealed at different temperature.
337

338 **3.5 Thermal analysis of the prepared xerogel catalysts**
339 The thermal stability of the prepared ZnO and Cu – ZnO by the fast sol–gel method was
340 studied by TGA and DTG as shown in Fig. 5a, b. For the ZnO, the weight loss of the xerogel
341 occurred principally in two steps. In the first step, weight loss (8 %) was in the range of 80–
342 178^{0}C, due to the dehydration of the absorbed surface water, as well as hydrate from the
343 remaining zinc acetate and methanol solvent. In the second step, weight loss occurred in the
344 range from 190 to 244^{0}c, which corresponds to 17 % due to the decomposition of tartaric
345 acid. In the last step, weight loss ranged from 284 to 482 ^{0}C due to the conversion of zinc
346 tartarate to zinc oxide and the percentage of weight loss was found to be 41.5 %. After 482
347 ^{0}C, no weight loss was observed and zinc oxide formed was further confirmed by XRD. On
348 the other hand, for Cu – ZnO, a total weight loss of 7.9 % was observed in all four steps, and
349 this is very low as compared with ZnO xerogel (64.5 %), indicating an increase in its stability
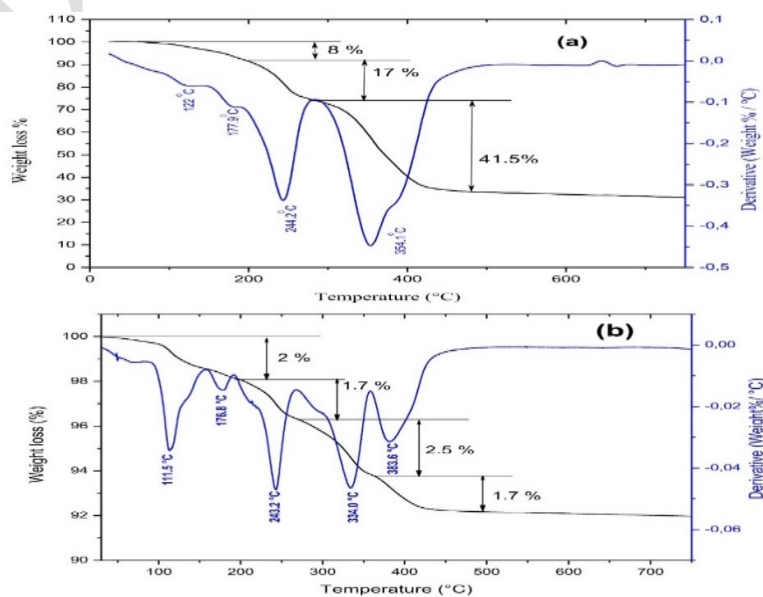350 due to the presence of Cu.
351

364
365
366   **Figure 5:** TG-DTG analysis of (a) ZnO and (b) Cu – ZnO xerogel powders.
367

368 **3.6 Characterization of ZnO and Cu – ZnO by Photocatalytic degradation of Malachite**
369 **Green**
370 The photocatalytic performances of ZnO and Cu-doped ZnO samples were investigated under
371 UV light through the degradation of Malachite Green (MG), as a model organic pollutant.
372 Figure 5 shows the photodegradation activity of ZnO annealed at 550 ^{0}c and Cu – ZnO
373 annealed at T_C of 250–550 ^{0}c photocatalysts. The results show that there is no degradation in
374 the absence of the photocatalyst. On the other hand, the photocatalytic activity of ZnO was
375 found to be very low: only 20 % of MG was degraded after 3h of irradiation. However, after
376 doping ZnO with copper significantly increased its photocatalytic efficiency towards the
377 degradation of MG. However, the efficiency of ZnO was significantly increased after doping
378 with copper. As observed in Fig. 5, the kinetics were well fitted to pseudo first order then, the
379 obtained values of the rate constant using Origin.8 software were plotted against the
380 annealing temperature. It's known that the photocatalytic activity is related to the surface area
381 of the photocatalyst. The present results were showed that the Cu-doping ZnO and the
382 annealing temperature have played a crucial role on the enhancement of the photocatalytic
383 efficiency by increasing the surface area. Nevertheless, this is not simply a question of
384 specific surface area and adsorption, despite the fact that adsorption is a very important step
385 in the photocatalytic process. Figure 6 shows the adsorption in the dark, which depends to the
386 nature of the catalyst. The most adsorbed quantity of the MG was found over the Cu-doped
387 catalyst annealed at T_C = 250 ^{0}C. This result is in a good agreement with the obtained specific
388 surface area value (35.10 m^2/g), but this catalyst was found to be less photoactive towards
389 MG degradation, among other Cu-doped catalysts. Itis also important to note that the
390 photocatalytic efficiency towards the degradation of MG with Cu – ZnO increased with
391 increase in annealing temperature and formation of a CuO phase on the surface. This clearly
392 demonstrates that photocatalytic activity depends on the annealing temperature rather than
393 particles size and surface area. Similarly, it was shown that the photocatalytic activity of a
394 catalyst is related to its microstructure, such as crystal plane, crystallinity, surface properties,
395 BET specific surface area [38]. Many studies have shown that the difference in photocatalytic
396 activity among all catalysts, not only related to the surface adsorption ability, but also to the
397 type and concentration of oxygen defects on the surface and/or surface layers. Two major
398 parameters can be affected by the annealing temperature: the increase in crystallinity and
399 decrease of surface OH groups. Normally, since photocatalysis is a surface phenomenon, the
400 decrease in surface OH groups may cause a loss in photocatalytic activity. However, the
401 highest photoactivity in terms of MG degradation rate or kinetic constant was obtained from
402 the catalyst annealed at the highest temperature (T_C = 550 ^{0}C) and with the lowest specific
403 surface area (8.66 m^2/g). Therefore, an optimal quantity of hydroxyl groups on the catalyst
404 surface in combination with a certain degree of crystallinity, and specific kinds of oxygen
405 defects on the surface and /or surface layers are required to achieve optimal photoactivity
406 [35]. In this study, the increase in photocatalytic activity of Cu - ZnO T_C = 550^{0}C may be
407 attributed to the good crystallinity and oxygen defects as reported for ZnO [39]. However, the
408 increasing crystallinity level with annealing temperature and the introduction of the native
409 defects in the catalyst crystal in the form of neutral (VO), singly charged (VO+) or doubly
410 charged (VO++) oxygen vacancies at higher annealing temperatures, may play a major role
411 in the enhancement of its photocatalytic efficiency [40]. It is well known that these defects in
412 the nanoparticles reduce the electron-hole recombination; hence increase the quantum yield
413 and thus, enhance the photocatalytic activity. Furthermore, a high concentration of oxygen

414 vacancies on the catalyst surface at higher annealing temperature and CuO phase can also
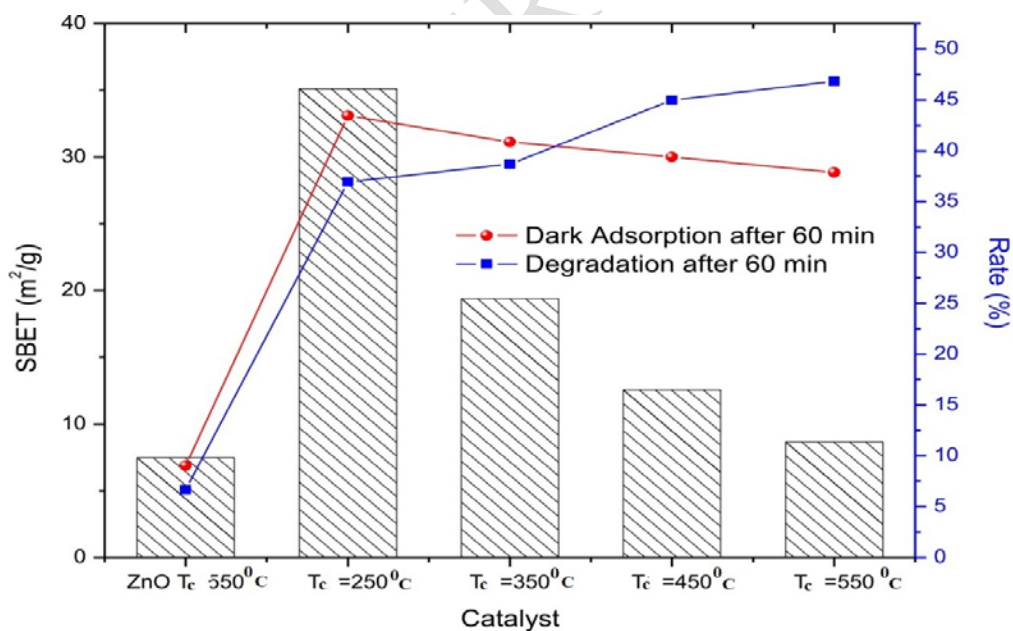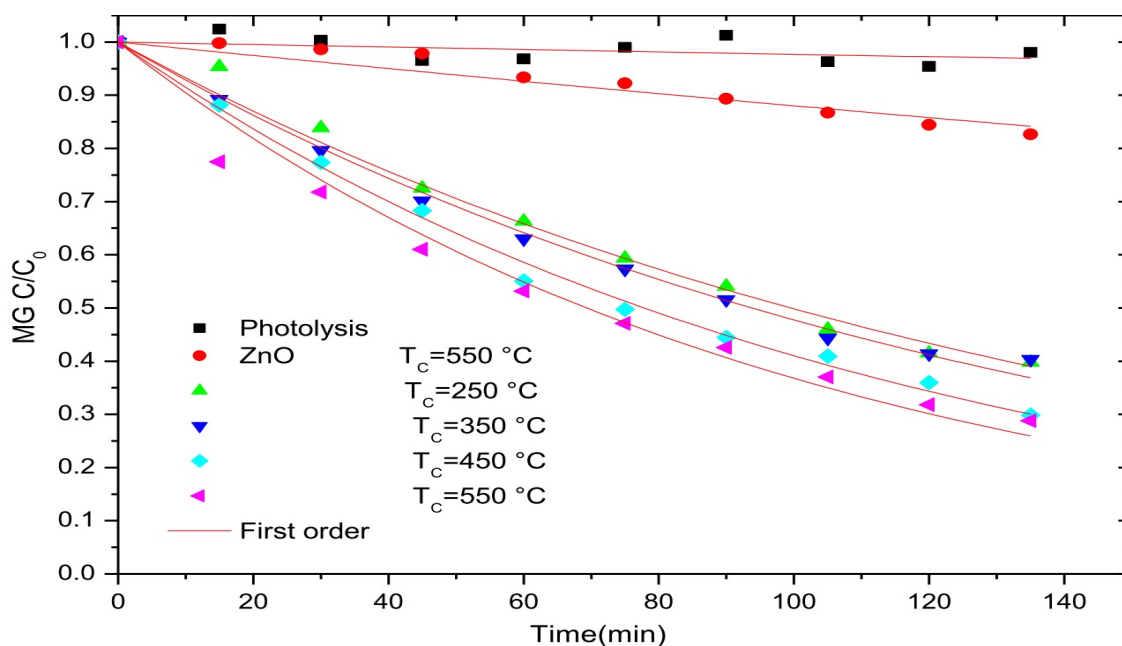415 serve as trap for electrons from the conduction band [41].
416

417
418
419
420
421
422
423
424
425
426
427
428
429
430
431
432
433
434
435
436

437 **Figure 6:** Effect of mesoporous catalysts on dark adsorption after60 min, and degradation of (MG) and (SBET
438 m^2/g)
439

3.6.1 Adsorption kinetics of MG dye

441 Kinetics adsorption were studied using 250 ml of MG solution with initial concentration of
442 300 mg/L and 750 mg of solid was added and stirred in the dark. A sample was withdrawn
443 every 15 min, diluted, centrifuged and residual concentration measured by spectrophotometer

444 [Labomed – UVS-2800] at a maximum wavelength of 618 nm. The quantity of MG adsorbed
445 per gram of catalysts at time (min) is calculated using following equation [42]:

446 $q_t = \frac{(C_0 - C_t)V}{m}$ (4)

447 Where q_t is the quantity of adsorbed MG per gram of adsorbent (catalysts)at time t, C_0 is the
448 initial MG concentration, Ct the concentration of MG at time t, V is the volume of the MG
449 solution (ml) and m is the mass of the solid used (mg). All the data was fitted using pseudo-
450 first order nonlinear Lagergren model [43]:

451 $q_t = q_e(1 - e^{-kt})$ (5)

452 This kinetics are shown in Figure.7 for the ZnO and the Cu – ZnO photocatalysts annealed at
453 different temperatures (T_C). As it can be seen all kinetics obey to the first order according to
454 Lagergren model (Equation 5) experimental data are represented by scatter points and
455 Lagergren simulation by continuous line. However, it can be deduced from Figure.7, stirring
456 the MG + catalyst suspensions must be maintained in the dark for at least60 min which
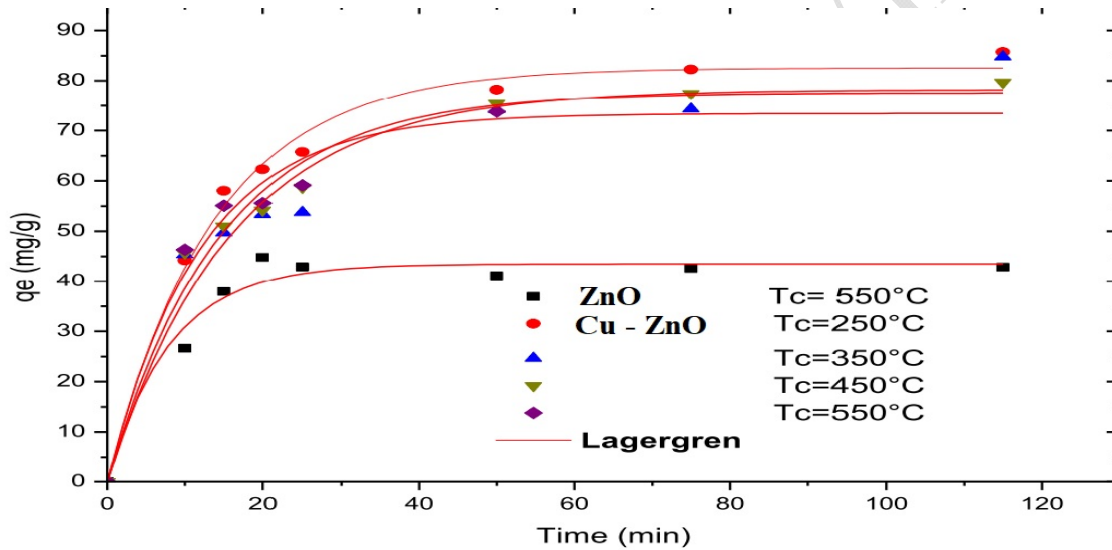457 represents the solid saturation time (t_{sat}) prior to the degradation reaction.

458
459

460
461 **Figure 7:**MG Adsorption kinetics on catalysts annealed at different temperatures and Lagergren simulation.
462
463

464 Figures.8 (a) and (b) show, the effects of annealing temperature on the apparent adsorption
465 kinetic constants (k_{ads}) and equilibrium adsorbed amounts (q_e) deduced from the Figure 7. by
466 the Lagergren simulation. For the same annealing temperature (T_C = 550°C), doping ZnO
467 with Cu decreases the rate of adsorption reaction Figures.8 (a) but in contrast the equilibrium
468 adsorbed amount (q_e) is approximately doubled (1.7 times higher; Figures.8 (b) which can be
469 explained by both: increasing of the specific surface area (1.15 times higher) and increasing
470 site numbers created by the presence of copper (1.4 times higher). On the other hand, the
471 adsorption rate seems to depend on both annealing temperature and specific surface area. In
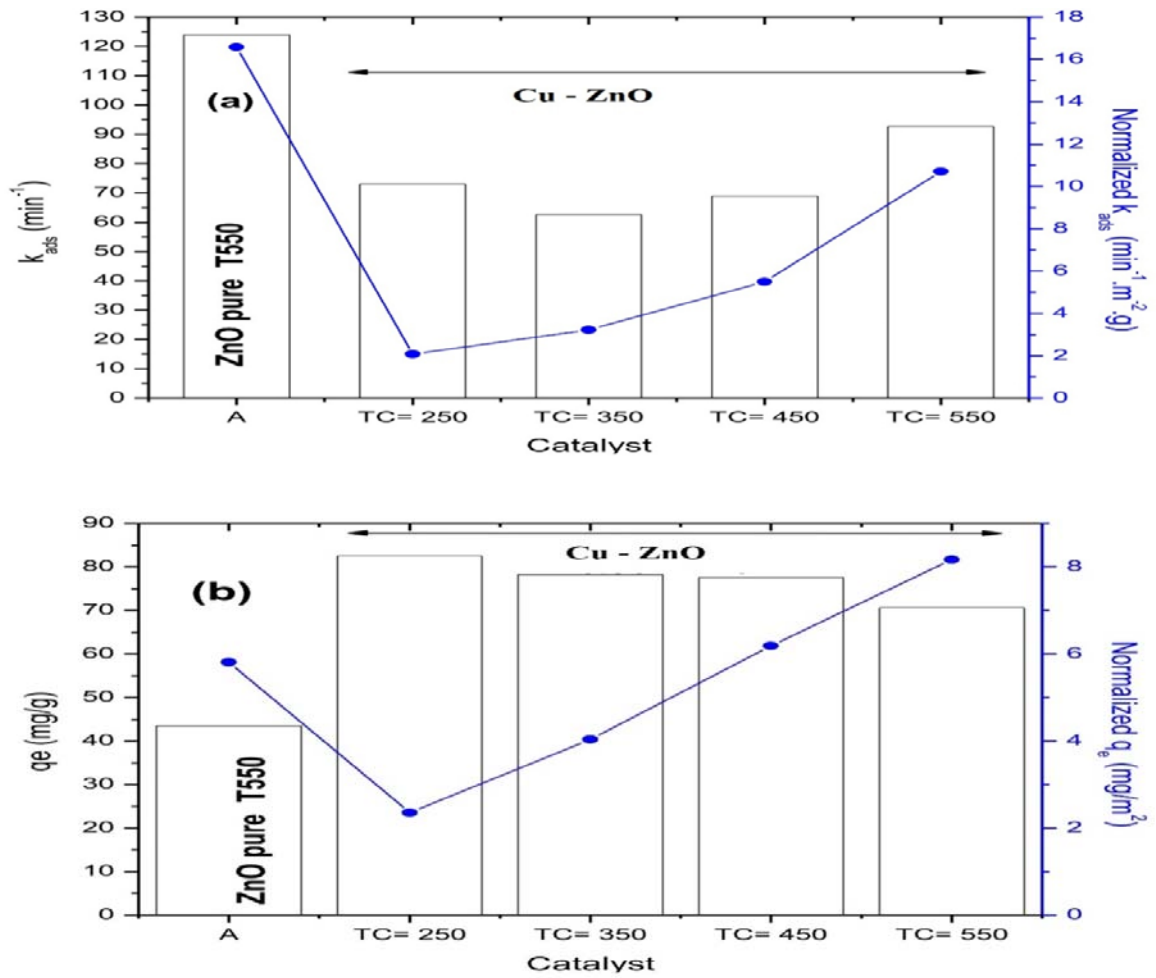472 deed the normalized adsorption rate constant increases gradually with the increase of T_C.

473 **Figure 8:** Effect of annealing temperature (a) on the MG adsorption kinetic constant and (b) on the equilibrium
474 MG adsorbed amount
475

476 **3.6.2 Photocatalytic degradation of MG mechanism**
477 When mixtures of MG aqueous solution and a suspension of photocatalyst were irradiated
478 with VU light, the green solution of MG markedly changed, as a result of the decomposition
479 of the free radicals formed in the solution. The photocatalytic activity mechanism of Cu-ZnO
480 can be understood as follows: The Cu doped ZnO resulted in the creation of intermediate
481 energy levels, which cause a delay in the recombination of charge carriers, thereby enhancing
482 the photocatalytic activity. Moreover, it can be noticed that the delay in the recombination of
483 charge carriers increases whenever the crystallinity of Cu –ZnO photocatalyst is improved by
484 the annealing temperature rise. In the mechanism of photodegradation of MG in the presence
485 of Cu –ZnO photocatalyst. The excitation of photocatalyst by UV light results to the
486 formation of electrone$_{CB}^-$in both Cu/ZnO and CuO conduction bands. The direct bandgap of
487 ZnO and ZnO/CuO is estimated by Tauc's formula, $(\alpha h v)^n = B \left(h v - E_g \right)$, where **B**
488 is a constant related to the material, **hv** is the photon energy in eV, **h** is Planck's constant, **Eg**
489 is the optical bandgap in eV, n is an exponent that can take a value of either 2 for a direct
490 transition or 1/2 for an indirect transition, and **α** is the absorption coefficient (in cm^{-1}) [44].
491 The electrons $e_{CB,CuO}^-$ are transferred to the Cu/ZnO conduction band and then convert
492 dissolved oxygen to super oxide radical.O_2^-. While the holes $h_{VB,ZnO}^+$and $h_{VB,CuO}^+$from the
493 CuO valence band level react with water to form the strongest oxidizing agent, hydroxide

494 free radical .OH. Both active species can decompose MG completely [45,46]. The
495 mechanism is schematically depicted in Fig. 9 and Scheme 1.
496

497
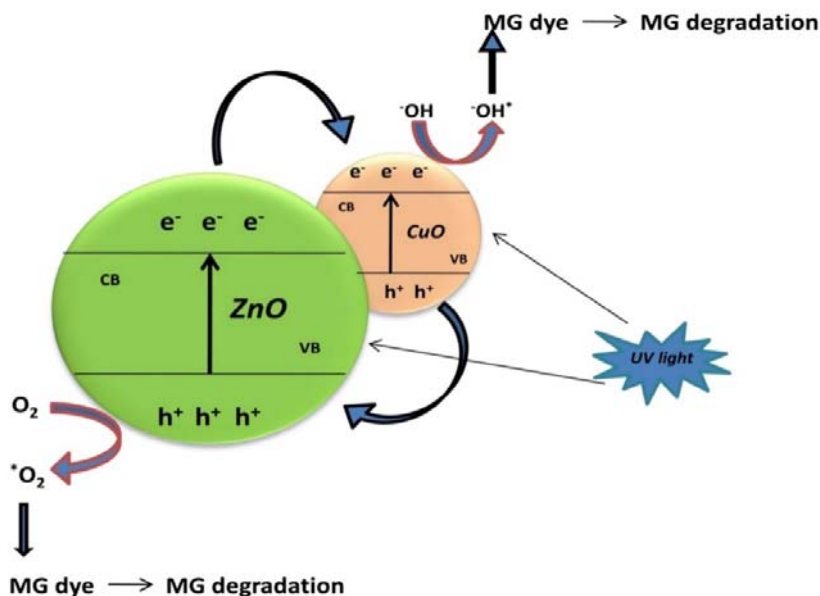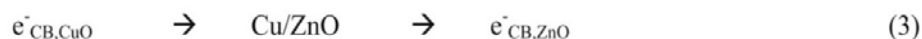498
499
500
501
502
503
504
505
506
507

508 **Figure 9**: photocatalyst mechanism leading to the photocatalytic degradation of MG.

509

510 $$CuO + h\nu \rightarrow e^-_{CB,CuO} + h^+_{VB,CuO} \quad (1)$$

511 $$Cu/ZnO + h\nu \rightarrow e^-_{CB,ZnO} + h^+_{VB,ZnO} \quad (2)$$

512
513 $$e^-_{CB,CuO} \rightarrow Cu/ZnO \rightarrow e^-_{CB,ZnO} \quad (3)$$

514 $$h^+_{VB,ZnO} \rightarrow CuO \rightarrow h^+_{VB,CuO} \quad (4)$$

515 $$e^-_{CB,ZnO} + O_2 \rightarrow {}^\circ O_2^- \quad (5)$$

516 $$h^+_{VB,CuO} + H_2O \rightarrow {}^\circ OH + H^+ \quad (6)$$

517 $${}^\circ O_2^- + H^+ \rightarrow {}^\circ O_2H \quad (7)$$

518 $${}^\circ O_2H + {}^\circ O_2^- + H^+ \rightarrow H_2O_2 + O_2 \quad (8)$$

519 $$e^-_{CB,ZnO} + H_2O_2 \rightarrow {}^\circ OH + OH^- \quad (9)$$

520 $${}^\circ O_2^- + MG \rightarrow \text{Degradation Products} \quad (10)$$

521 $${}^\circ OH + MG \rightarrow \text{Degradation Products} \quad (11)$$

522
523

524 **Scheme 1** Proposed MG degradation mechanism.

525

526 Figure.10 shows the effects of annealing temperature on the main properties of, prepared,
527 catalysts: Several correlations can be observed as for example the decrease in the specific
528 surface area due to a sintering phenomenon linked to the increase in temperature, which
529 increases the size of the crystallites by aggregation and confirms the effect on the surface.
530 However, it is important to note that the degradation of MG increases with the annealing
531 temperature despite the drop in specific surface proving that the photocatalysis is not, mainly,
532 due to the adsorptive capacity of the catalyst.

533
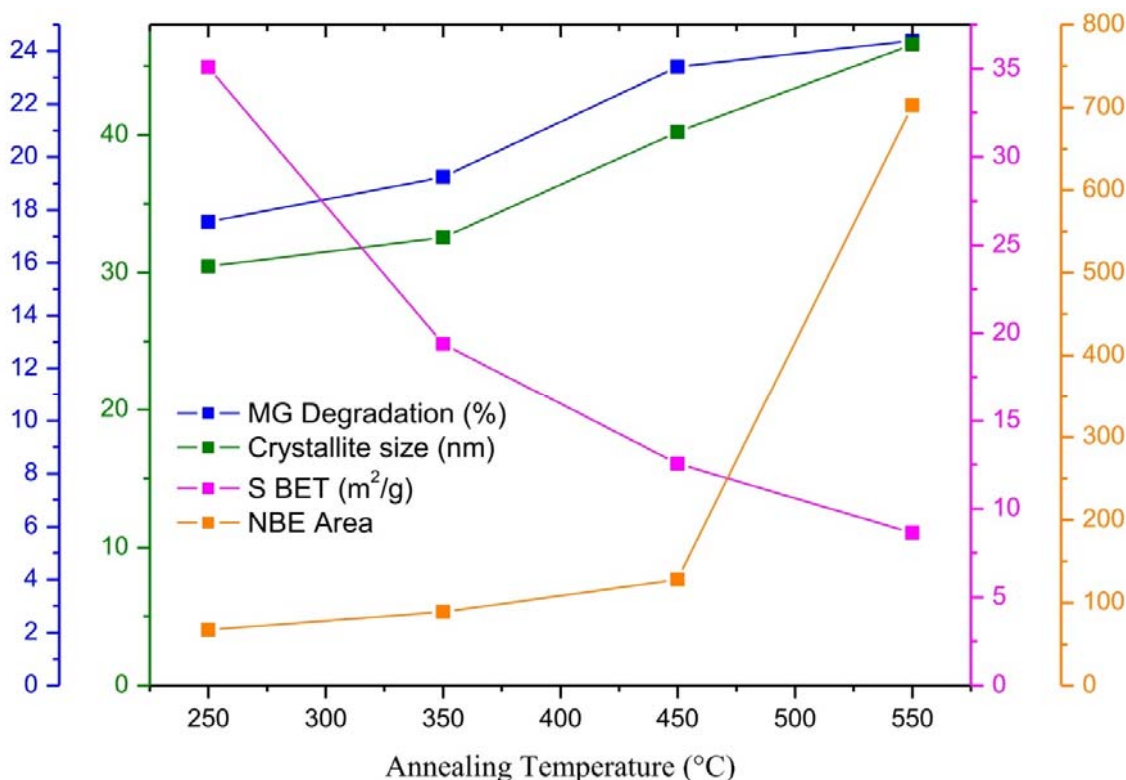
534 **Figure 10**: Dependences and correlation between NBE area, SBET and crystallite size and MG degradation on
535 the annealing T_c
536

537 **3.7 Optical Properties**
538 The optical transmission spectra of all samples in the visible region is a very important factor
539 in many applications. So, measured at room temperature are illustrated in Fig. 11. All
540 transmission spectra indicate sharp absorption edge. Moreover, as Cu composition increases,
541 the transmission spectra exhibit the obvious blue shift of absorption edge of an optical band
542 gap of the film and highly transparent within a visible region with increasing Cu composition.
543 From the graph it is seen that the values of transmittance are high in the visible and IR region
544 and it is minimum in the UV region. These spectra show high transmittance near about 75 -
545 85% in the wavelength range from 400-1100 nm. For direct transition the observed optical
546 band gap depends on the doping concentration and varies from 3.21 eV to 3.05 eV which is
547 shown in table 3. Similar result was also reported by Lee, H. J. et al [47]. The variation of
548 direct band gap energies with different doping concentration of Cu is shown in Fig.9 with
549 wavelength range 300 nm -1100 nm. Table 3 refer to variation of band gap of Cu ZnO thin
550 films with different doping concentration of Cu. The optical absorption spectra are shown in
551 fig. 12 with wavelength range 300 nm - 1100 nm. The figures show the variation of

552 absorbance with the doping concentration of copper. From the figure it is seen that the optical
553 absorption decreases with the doping concentration of copper of the Cu - ZnO thin films [48].
554 These spectra show high absorbance in the wavelength range from 300-400 nm. The optical
555 band gap can be determined by analyzing the transmission data using the classical relation
556 [49],

557 $$\alpha h v = A \ (h v - E_g)^n \tag{3}$$

558 where, A is a constant, "$h \ v$" is the photon energy and "E_g" is the optical band gap of the
559 semiconductor and "n" is index related to the density of states for the energy band and is
560 determined by the nature of optical transition involved in the absorption process. It is
561 observed that small amount of Cu present in the films greatly affects the optical band gap of
562 ZnO. The band gap decreases as the Cu concentration increases. Researcher think that this
563 shift of the band gap with the Cu incorporation interpreted as mainly due to the sp-d
564 exchange interactions between the band electrons and localized d electrons of the Cu^{+2} ions
565 substituting Zn ions. The s-p and p-d exchange interactions give rise to a negative and a
566 positive correction to conduction and valance band edges, leading to narrowing the band gap
567 [50]. The nature of this variation in the band gap energy may be useful to design a suitable
568 window material in fabrication of solar cells, means this thin-film technologies, that are still
569 in an early stage of ongoing research or with limited commercial availability, are often
570 classified as emerging or third generation photovoltaic cells and include, organic, dye-
571 sensitized, and polymer solar cells, as well as quantum dot, copper zinc, nanocrystal,
572 micromorph and perovskite solar cells. The variation of direct band gap energies with
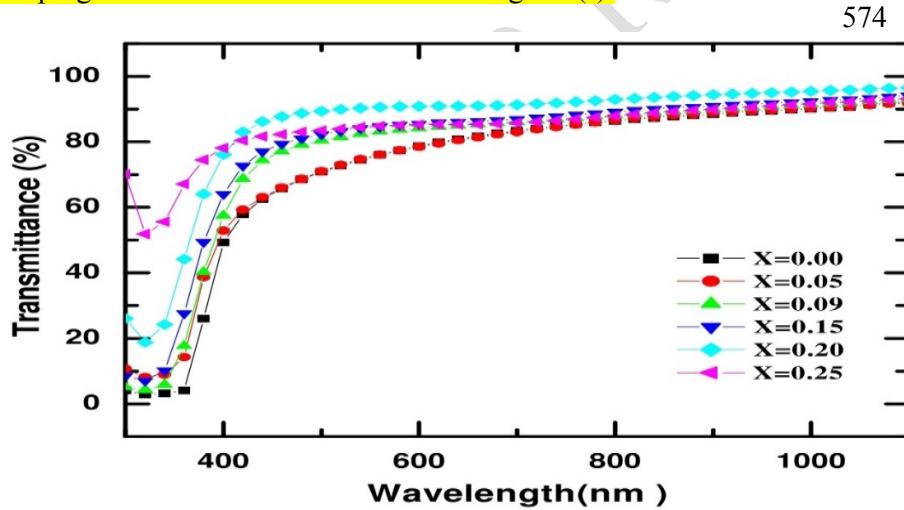573 different doping concentration of Cu is shown in fig. 13 (f).

574

585
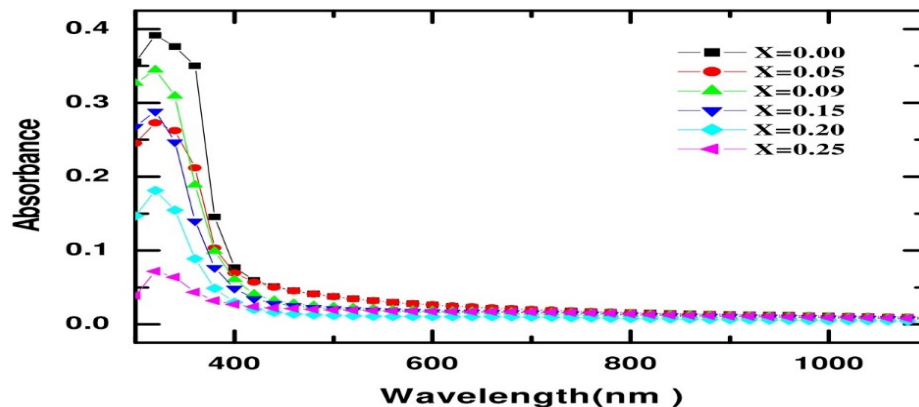586 **Figure 11:** Variation of optical transmittance with wavelength of Cu ZnO thin films for different concentration.
587

588
589
590
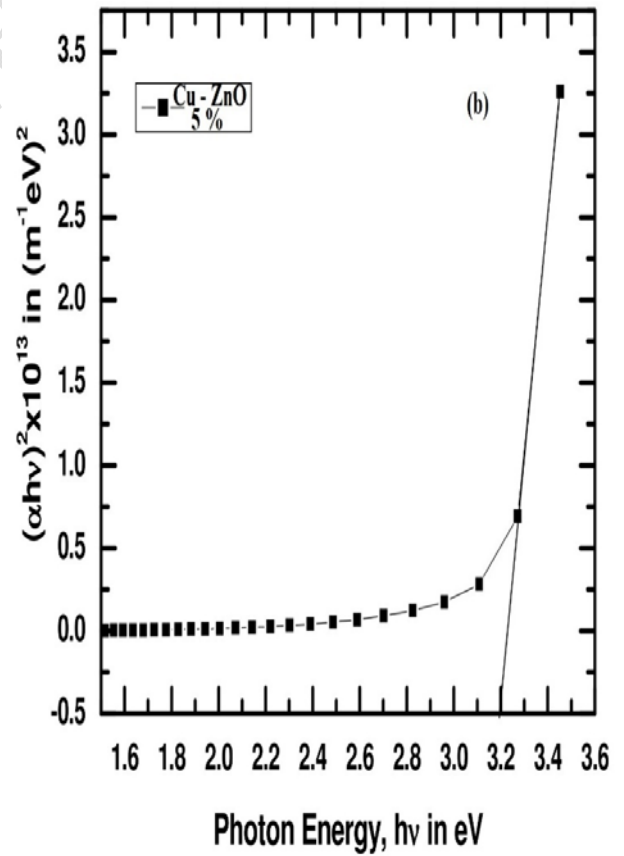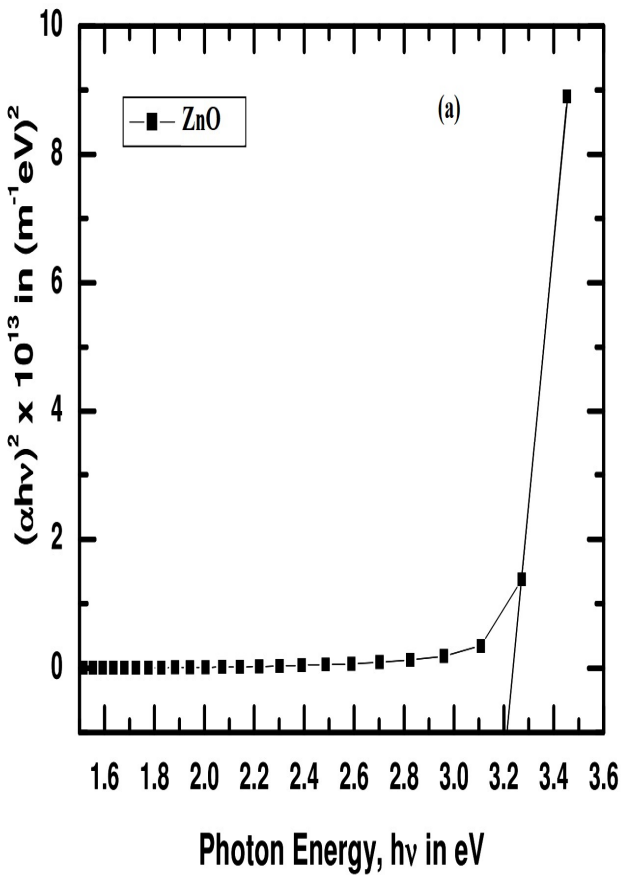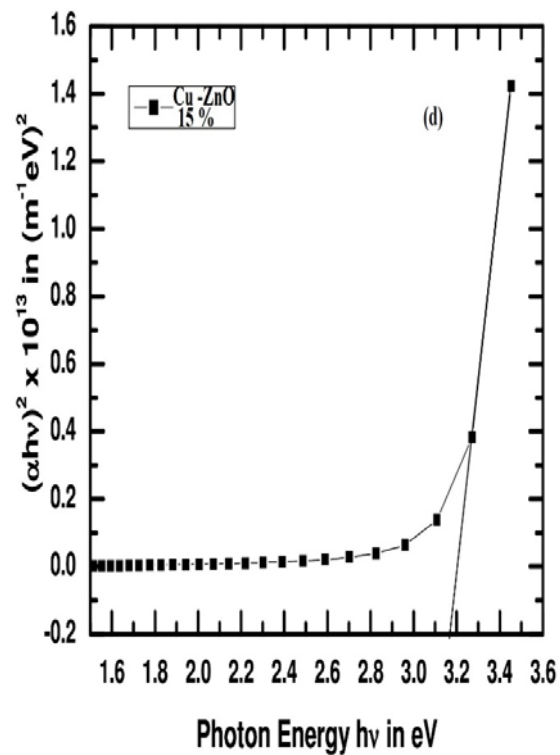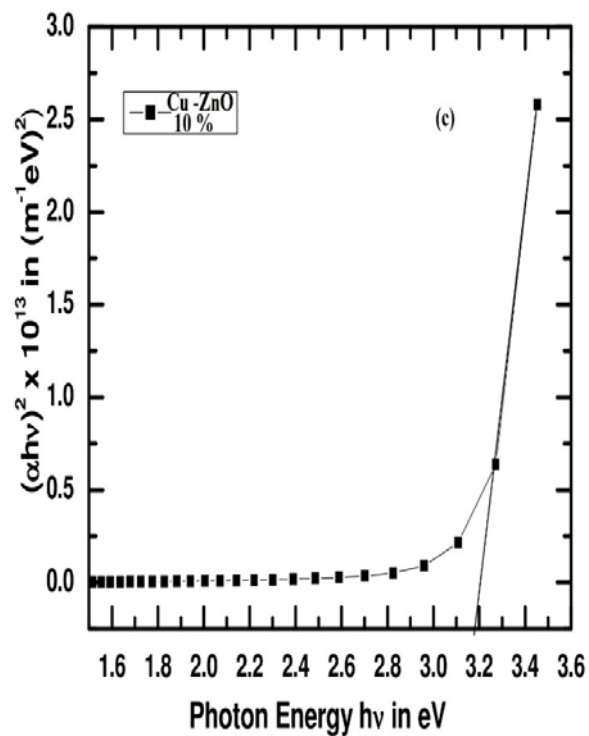591
592
593
594
595
596

597
598
599   **Figure 12:** Variation of optical absorption with wavelength of Cu ZnO thin films for different concentration.
600

601

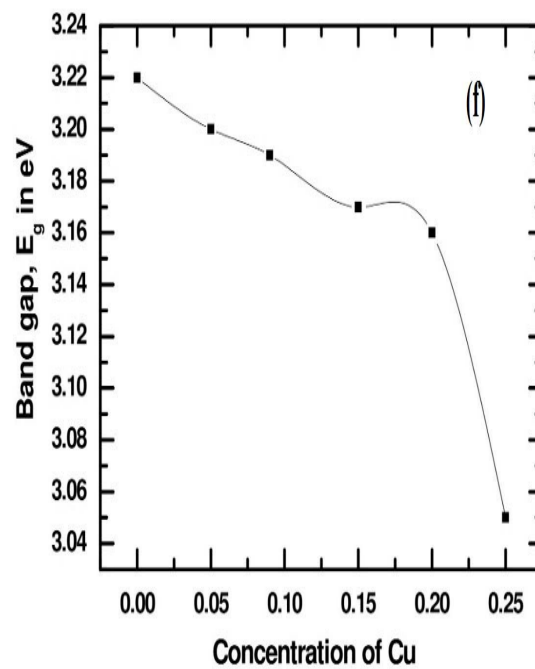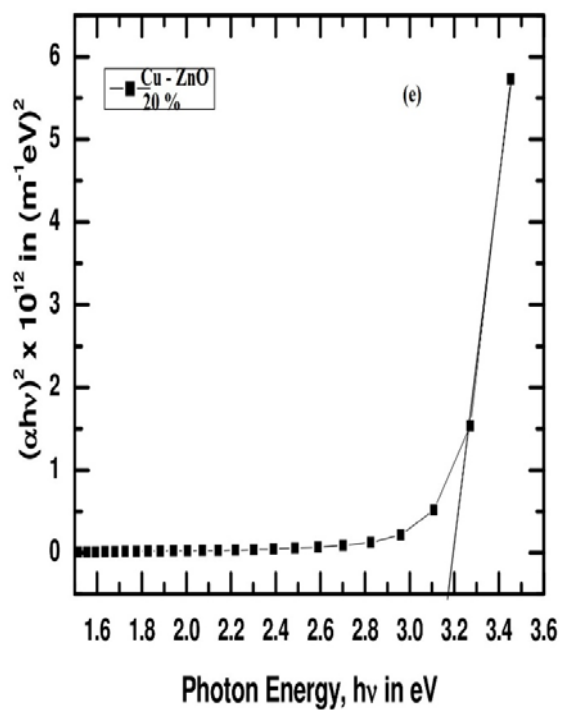602   **Table 3:** Band gap of Cu ZnO thin films with different doping concentration of Cu.

Sample	Concentration of Cu (%)	Direct band gap E_g in eV
Cu ZnO	0	3.21
	5	3.20
	10	3.19
	15	3.17
	20	3.16
	25	3.05

603

604

605

606

607

631
632
633
634

637
638
639

640 **Figure 13:** Variation of $(\alpha h \nu)^2$ with photon energy for(a) ZnO. (b) 5% (c), 10%, (d), 15% and (e) 20% Cu
641 doped ZnO thin film. (f) Band gap energies with concentration of Cu for Cu ZnO thin films
642

3.8 Photoluminescence

644 The technique of photoluminescence excitation has become a standard one for obtaining
645 information on the nanostructures. The photoluminescence excitation technique involves
646 scanning the frequency of the excitation signal and recording the emission within a very
647 narrow spectral range. In this study, the photoluminescence (PL) spectra of ZnO
648 nanoparticles were estimated, to explore the effect of Cu-doping and annealing temperature
649 on its optical properties. Figure 14 shows the emission spectrum of ZnO and Cu - ZnO
650 catalysts, using an excitation wavelength of 325 nm at room temperature. The
651 photoluminescence (PL) emission was observed for all the samples (T_C = 250–550 ^{0}C)
652 covering the range: from a short wavelength of 350 nm to a long wavelength of 550 nm. As
653 the annealing temperature increased at 550^{0}c, all UV and visible luminescence also increased.
654 The increase in UV emission may be ascribed to the improvement in observed crystalline
655 quality due to annealing. The enhancement in blue emissions intensities is likely due to the
656 strong exchange interactions between Zn and the second phase formed by Cu, after annealing
657 of the sample. The first one, which originates from the recombination of free exciton [51], is
658 clearly observed for ZnO at 379 nm. Thus, Cu -ZnO was annealed at the highest temperature
659 T_C = 550 ^{0}C at 385 nm, and this may be attributed to exciton-related near-band edge emission
660 (NBE). The second peak was observed according to the annealing temperature T_C at 417,
661 421, 428.5 and 430 nm, which corresponds to the blue emission [52]. As can be seen, the
662 second peak seems to be observed only for Cu – ZnO   catalysts, while the intensity of both
663 peaks depends strongly on the annealing temperature.   As the annealing temperature
664 increases, the ultraviolet emission peak of the ZnO and Cu – ZnO catalysts, gradually,
665 increases especially for T_C = 550°C. This increase was also observed for the blue emission
666 peak for all annealing temperatures. For further understanding of the PL analysis, Figure.15.
667 (a)-(e) shows that all PL spectra are well fitted with a Gaussian function (the lowest
668 correlation coefficient is 99.4%). For ZnO the de-convoluted PL spectrum (Figure.15. (a))
669 shows three peaks: two UV emission peaks of approximately the same intensity at 373 and
670 389 nm corresponding to the near-band emission of ZnO [53]and a violet emission peak at
671 410 nm with lower intensity. The effect of Cu doping can be seen at the same T_C = 550°C. By
672 comparison of Figure.15(a) and (b), it was observed that there is a red-shift of approximately
673 5 nm in the Cu-doped sample, which may correspond to a reduction in ZnO band gap due to
674 Cu doping and the substitution of Cu ions into the Zn sites in the lattice as reported in the
675 XRD study. Xu et al. [54] and Udayabhaskar et al. [55], reported similar results on Cu-doped
676 ZnO, Ni-doped ZnO and Ca-doped ZnO materials, respectively.   It was noticed that the
677 violet peak at 410 in the ZnO completely disappeared this may be attributed to the defects
678 and/or lattice imperfections of the ZnO sample, which can be removed by low-temperature
679 thermal annealing. However, it seems that the peak was replaced by the two blue emission
680 peaks in the Cu – ZnO   mesoporous catalysts. The observation of visible emissions may be
681 related to intrinsic defects in ZnO and their enhancement in the presence of Cu ions induced a
682 poorer crystallinity and greater level of structural defects, which can be attributed to the more
683 intrinsic defects introduced by Cu ion incorporation into the ZnO lattice. This result is in line
684 with the above XRD findings. Xu et al. [54] related similar results to Raman observations
685 regarding the defects gradually generated with the Cu doping ratio. The effect of annealing
686 temperature T_C and its comparison is shown in Table 4 and fig 15 (a-e). As the annealing
687 temperature increased from 250 to 550°C, all UV and visible luminescence increased. The
688 increase in UV emission may be ascribed to the improvement in observed crystalline quality
689 due to annealing. The enhancement in blue emissions intensities is likely due to the strong
690 exchange interactions between Zn and the secondary phase formed by Cu, after annealing of

691 the sample. Certainly, thermal annealing can provide more energy for the substitution of Zn
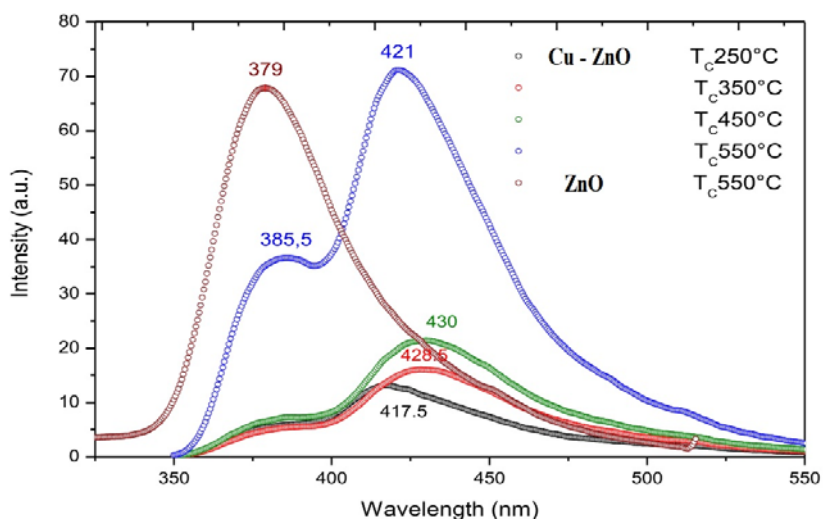692 atom sites by Cu atoms into the lattice of ZnO.
693

694
695
696
697
698
699
700
701
702
703
704
705
706
707
708
709
710
711
712
713
714

715 **Figure 14:**PL Spectra of the ZnO annealed at 550 ^{0}c and Cu-ZnO annealed at different temperatures at
716 excitation wavelength 325nm^{0}c.
717
718 **Table 4:** Photoluminescence Emission Values of pure and Cu-doped ZnO deduced from de-convolution by
719 Gaussian function of PL spectra.
720

Catalysts	Near band edge , NEB (nm)	NEB intensity (a.u)	Blue emission (nm)
ZnO, T_c = 550 ^{0}c	373- 389	32.40- 31.41	410(violet)
Cu – ZnO, T_c = 550 ^{0}c	378	27.87	423. 45
T_c = 450 ^{0}c	379	4.89	429. 46
T_c = 350 ^{0}c	379	3.44	429. 46
T_c = 250 ^{0}c	378	3.13	419. 45
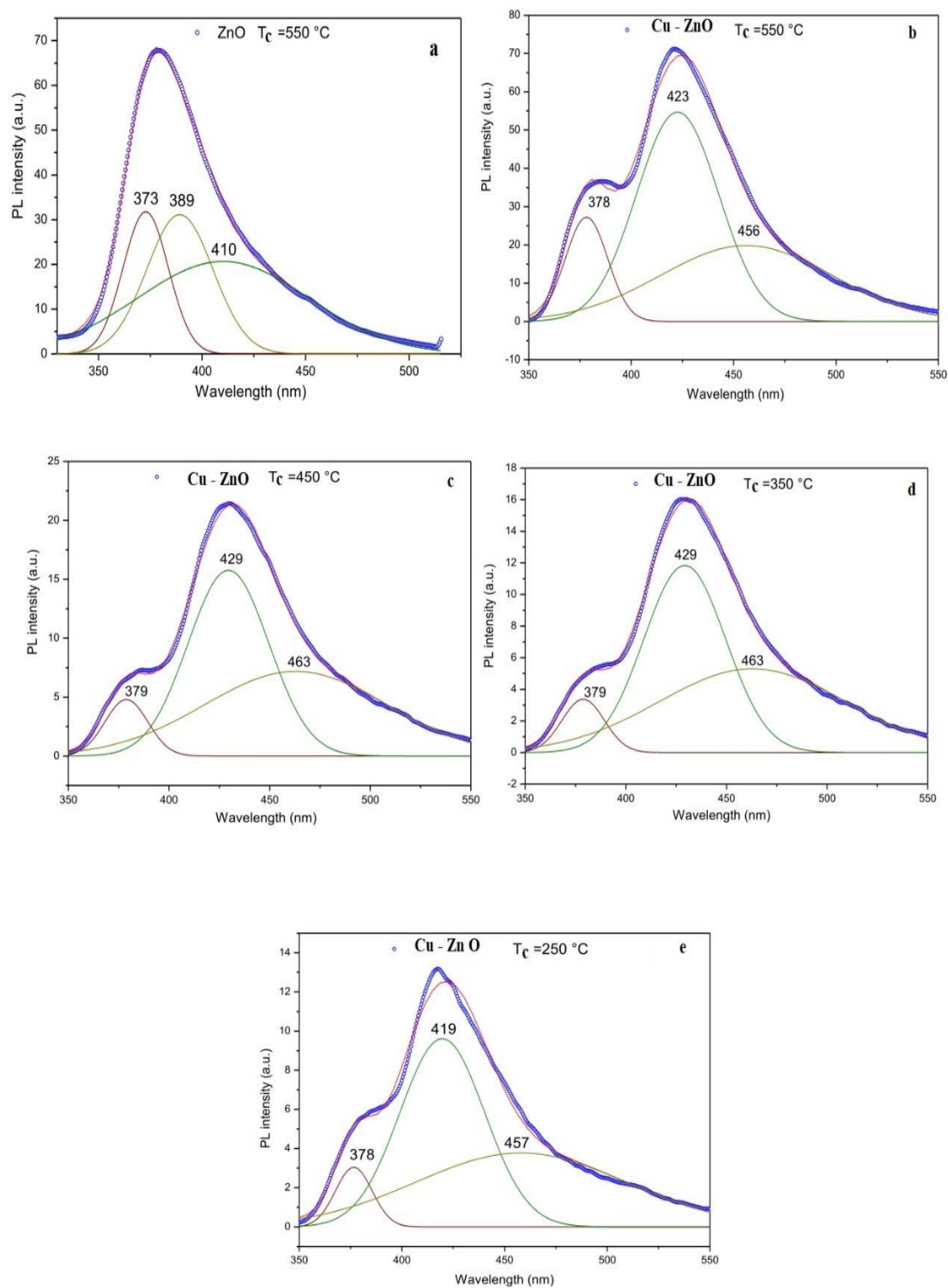
721
722
723 **Figure 15:** PL emissions spectra of ZnO $T_C = 550\ {}^0C$, (b) Cu – ZnO $T_C = 250\ {}^0C$, (c) $T_C = 350\ {}^0C$, (d) $T_C = 450^0$
724 C and (e) $T_C = 550\ {}^0C$ NPs using the excitation wavelength at 325 nm.
725

726

3.9 Electrical Properties

Resistivity of the prepared ZnO and Cu doped ZnO thin films have been measured by van-der Pauw method [56]. The resistivity measurement has been performed over a range from room temperature to 440 K. During the measurement, the temperature increased slowly as a result the whole film is heated with uniform temperature. The variation of resistivity with temperature for films and resistivity gradually decreases with the increase of temperature, which indicates the semiconducting nature of the materials is shown in Fig. 16. The electrical resistivity of ZnO was increased by doping Cu indicating the acceptor like behavior of the Cu dopant. The four coordinated Zn, Cu and Cu cations have ionic radii of 0.06, 0.06 and 0.057 nm respectively, with stable electronic configuration, Zn^{2+} $(3d^{10})$, Cu^{2+} $(3d^9)$ and $Cu^+(3d^{10})$. Diffusion at high firing temperature may lead defect reactions in which Cu^{2+} cations substitute Zn^{2+} cations in the wurtzite unit cell of ZnO. The stability of the coulomb forces of the interactions between the acceptor defect $(Cu^{1+}Zn)$ and intrinsic ZnO donors may occur by capture of an electron from the lattice.
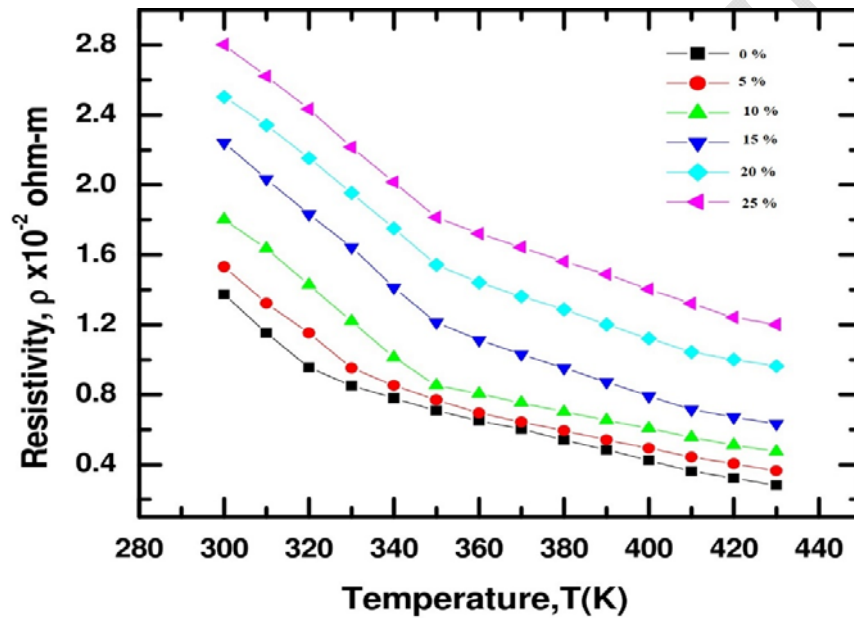

Figure 16: Variation of electrical resistivity with temperature for Cu ZnO thin films

The variations of electrical conductivity with temperature for Cu ZnO thin films are shown in Fig. 17. From the figure it is seen that the conductivity increases with the increase of temperature. This type of variation indicates the semiconducting behavior of the films. The conductivity decreases with the increasing of Cu concentration [47]. Incorporation of Cu into ZnO reduces its conductivity as Cu introduces deep acceptor level and it traps electrons from the conduction band.
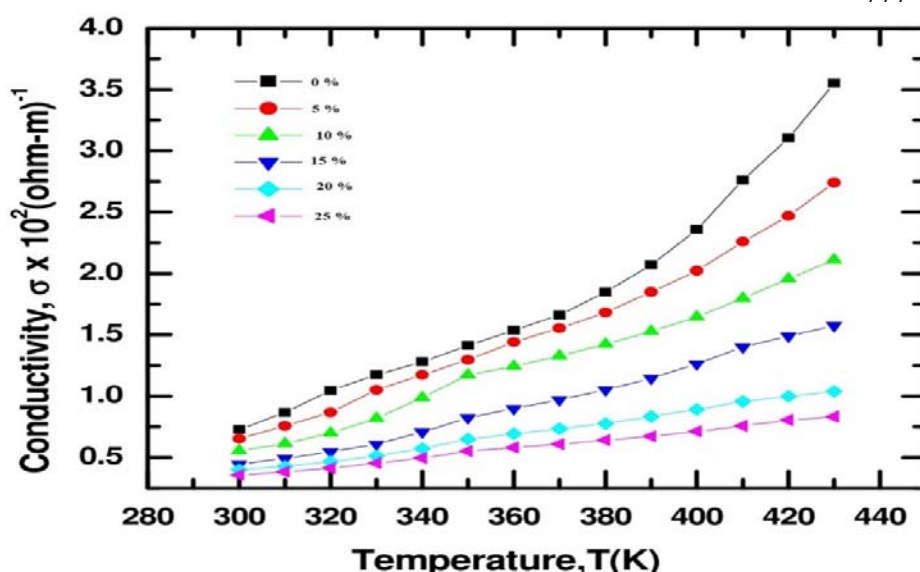
Figure 17: Variation of electrical conductivity with temperature for Cu ZnO thin films

4. Conclusions

In the present work, Zinc oxide and Cu-doped ZnO thin films were synthesized by a sol–gel method in the presence of tartaric acid. The obtained powders were annealed at different temperatures. XRD studies confirmed the dominant presence of hexagonal wurtzite ZnO with the formation of monoclinic CuO phase on the surface of ZnO. Films of different doping concentration of Cu were deposited on glass substrate. it was shown that specific surface area decreases with annealing temperature due to the occurrence of the aggregation phenomenon. The photocatalytic ability showed that the catalyst activity was influenced by both different doping concentration of Cu loading on ZnO and annealing temperature. The Cu – ZnO catalyst annealed at 550 ^{0}C exhibited the highest photocatalytic activity due to the interlacing of several factors such as the efficient charge separation as proven by the PL spectra, the enhancement of crystallinity and the introduction of the native defects in the catalyst crystal in the form of neutral (VO), singly charged (VO$^+$) or doubly charged (VO^{++}) oxygen vacancies. Moreover, the CuO phase on the surface resulted in delayed recombination charge and increased the photocatalytic activity of catalysts at a higher temperature. Various optical constants such as absorbance, transmittance of the films have been studied for the as-deposited films are recorded in the wavelength ranges from 300 to 1100 nm. The values of transmittance are high in the visible and IR region and it is minimum in the UV region. Absorbance decreases with higher percentage of Cu concentration. The band gap of the films varied 3.21 to 3.05 eV. The increase in the Cu incorporation in the film results in the overall decrease in the refractive index. The electrical resistivity measurements were made on number of films from the room temperature up to 430K. The figure shows that the resistivity gradually decreases with the increase of temperature, which indicates the semiconducting nature of the materials. Resistivity also increases with the increasing doping concentration. The conductivity decreases with the increasing of Cu concentration. Incorporation of Cu into ZnO reduces its conductivity as Cu introduces deep acceptor level and it traps electrons from the conduction band.

Competing Interests

The author declares that there are no personal, organizational or financial conflicts of interest.

830   **References**
831   [1] T. Kavitha and H. Yuvaraj J,"A facile approach to the synthesis of high-quality NiO
832   nanorods: electrochemical and antibacterial properties",*J. Mater. Chem.*, 2011,21, 15686-
833   15691.DOI: 10.1039/C1JM13278D
834   [2] C.-C Wu and W.-C Shih, "Development of a highly transparent, low-resistance lithium-
835   doped nickel oxide triple-layer film deposited by magnetron sputtering", *Chem.
836   Commun.,*2017,53, 1634–1637.DOI: 10.1039/C6CC08738H
837   [3] T. Karali, N. Can, L. Valberg, A.L. Stepanov, P.D. Townsend, Ch. Buchal, R.A. Ganeev,
838   A.I. Ryasnyansky, H.G. Belik, M.L. Jessett, C. Ong, "Optical properties and luminescence of
839   metallic nanoclusters in ZnO: Cu", *Physica B: Condensed Matter*.2005, 363, 88-95.
840   doi.org/10.1016/j.physb.2005.03.006
841   [4] Vikas Sharma, Inderjeet Singh, Amreesh Chandra, "Hollow nanostructures of metal
842   oxides as next generation electrode materials for supercapacitors", *Scientific Reports*, 2018,
843   volume 8, Article number: 1307 , doi.org/10.1038/s41598-018-19815-y
844   [5] Khan Mamun Reza, ASW Kurny, Fahmida Gulshan, "Parameters affecting the
845   photocatalytic degradation of dyes using TiO_2: a review", *Applied Water Science,* July 2017,
846   Volume 7, Issue 4, pp 1569–1578. https://link.springer.com/article/10.1007/s13201-015-
847   0367-y.
848   [6] M. El-Hilo, A. A. Dakhel, A.Y. Ali-Mohamed, "Room temperature ferromagnetism in
849   Nanocrystalline Ni-doped ZnO synthesized by co-precipitation", *Journal of Magnetism and
850   Magnetic Materials*, 2009, 321, 2279–2283. doi.org/10.1016/j.jmmm.2009.01.040
851   [7] M.H. Mamat, M.Z. Sahdan, Z. Khusaimi, A. Zain Ahmed, S. Abdullah, M. Rusop,
852   "Influence of doping concentrations on the aluminum doped zinc oxide thin films properties
853   for ultraviolet photoconductive sensor applications", *Optical Materials*, 2010, 32, 696–699.
854   doi.org/10.1016/j.optmat.2009.12.005
855   [8] J. H.Li, Y.C. Liu, C.L. Shao, X.T. Zhang, D.Z. Shen, Y.M. Lu, J.Y. Zhang and X.W. Fan,
856   "Effects of thermal annealing on the structural and optical properties of $Mg_x Zn_{1-x} O$
857   nanocrystals", *J Colloid Interf Sci*., 2005, 283, 513-517, 10.1016/j.jcis.2004.09.011
858   [9] M. Krunks, T. Dedova, and I.O. Açik, "Spray pyrolysis deposition of zinc oxide
859   nanostructured layers", *Thin Solid Films*, 2006, 515, 1157-1160.
860   doi.org/10.1016/j.tsf.2006.07.134
861   [10] M. Ramakrishna Murthy, E. Venkateshwar Rao,"Ion-beam modifications of the surface
862   morphology and conductivity in some polymer thin films", *Bulletin of Materials Science*,
863   2002, 25, 403–406, doi.org/10.1007/BF02708018
864   [11] M. M. Abdelrahman, M. Osman, A. Hashhash, "Electrical properties of irradiated PVA
865   film by using ion/electron beam", *Progress of Theoretical and Experimental Physics*, 2016,
866   2016, doi.org/10.1093/ptep/ptv178
867   [12] Z. A. Fekete, E. Wilusz, F. E. Karasz, and C. Visy, "Ion beam irradiation of conjugated
868   polymers for preparing new membrane materials-A theoretical study", *Separation
869   Purification Technology*, 2007, 57, 440 – 443, doi.org/10.1016/j.seppur.2006.04.014
870   [13] K. Makuuchi and S. Cheng, "Radiation Processing of Polymer Materials and its
871   Industrial Applications" (Copyright © 2012 John Wiley & Sons, Inc.). Online ISBN:
872   9781118162798. doi.org/10.1002/9781118162798.fmatter
873   [14] Sahbeni K, *et al*, "Annealing Temperature Effect on the Physical Properties of Titanium
874   Oxide Thin Films Prepared by the Sol-Gel Method", *Journal of Physical Chemistry &
875   Biophysics,* 2017, 7: 257, https://www.omicsonline.org/open-access/annealing-temperature-
876   effect-on-the-physical-properties-of-titaniumoxide-thin-films-prepared-by-the-solgel-method-
877   2161-0398-1000257.pdf
878   [15] A. Abdolahzadeh Ziabari, F.E. Ghodsi, "Optical and Structural Studies of Sol-Gel
879   Deposited Nanostructured CdO Thin Films: Annealing Effect", *ACTA PHYSICA POLONICA
880   A,* 2011, 120, http://przyrbwn.icm.edu.pl/APP/PDF/120/a120z3p31.pdf

881 [16] G. L. Agawane, S. W. Shin, S. A. Vanalaka, Jin Hyeok Kim, "Synthesis of simple, low
882 cost and benign sol–gel Cu$_2$ZnSnS$_4$ thin films: influence of different annealing atmospheres",
883 *J Mater Sci: Mater Electron,* 2015, 26, 1900 – 1907, DOI: 10.1007/s10854-014-2627-2
884 [17] Kai Loong Foo, Uda Hashim, Kashif Muhammad, Chun Hong Voon, "Sol–gel
885 synthesized zinc oxide nanorods and their structural and optical investigation for
886 optoelectronic application", *Nanoscale Res Lett.*, 2014, 9, 10.1186/1556-276X-9-429
887 [18] Ü. Özgür et al, "A comprehensive review of ZnO materials and devices", *J. Appl. Phys.*
888 98, 041301-103 (2005); https://doi.org/10.1063/1.1992666
889 [19] Vinod Kumar et al, "Rare Earth Doped Zinc Oxide Nanophosphor Powder: A Future
890 Material for Solid State Lighting and Solar Cells", *ACS Photonics*, 4 (11) 2613-2637 (2017);
891 https://10.1021/acsphotonics.7b00777
892 [20] Vinod Kumar et al, "Synthesis and characterization of aluminum–boron co-doped ZnO
893 nanostructures", *Material Research Bulletin* 48, 362 (2013);
894 https://doi.org/10.1016/j.materresbull.2012.10.042
895 [21] Rabia Qindeel et al, "Characterizations of multilayer ZnO thin films deposited by sol-gel
896 spin coating technique", *Results in Physics*, Volume 7, 2017, Pages 651-655.
897 https://doi.org/10.1016/j.rinp.2016.12.029
898 [22] R. Amari et al, "Structural, Optical and Luminescence Properties of ZnO Thin Films
899 Prepared by
900 Sol-Gel Spin-Coating Method: Effect of Precursor Concentration", *CHIN. PHYS. LETT.* Vol.
901 35, No. 1 (2018) 01680. https://10.1088/0256-307X/35/1/016801
902 [23] Vinod Kumar et al, "Deep level defect correlated emission and Si diffusion in ZnO:
903 Tb3^{+} thin films prepared by pulsed laser deposition", J. Colloid and Interface Science 465,
904 295 (2016). https://doi.org/10.1016/j.jcis.2015.12.007
905 [24] Kaniz Naila Tonny et al, "Electrical, optical and structural properties of transparent
906 conducting Al doped ZnO (AZO) deposited by sol-gel spin coating", *AIP Advances*, 8,
907 065307 (2018); https://doi.org/10.1063/1.5023020
908 [25] Ziaul Raza Khan, "Sol-Gel Derived Cds Nanocrystalline Thin Films: Optical and
909 Photoconduction Properties", *Materials Science-Poland*, Volume 36: Issue 2, Jun 2018,
910 Pages 235–241, https://doi.org/10.1515/msp-2018-0028
911 [26] S. Sugi, Usha Rajalakshmi, J. Shanthi, "Photocatalytic degradation Efficiency of
912 Cu$_X$Zn$_{1-X}$O composite", *Optik* , 2017, 131, 406-413, doi.org/10.1016/j.ijleo.2016.11.030.
913 [27] Marco Laurenti, Valentina Cauda, "Porous Zinc Oxide Thin Films: Synthesis
914 Approaches and Applications", *MDPI Coatings* 2018, 8(2), 67;
915 https://10.3390/coatings8020067
916 [28] Kadam L. D., Patil P. S., "Thickness-Dependent Properties of Sprayed Cobalt Oxide
917 Thin Films" *Materials Chemistry and Physics*, Vol. 68, pp 225–232,
918 2001.https://doi:10.1016/s0254-0584(00)00367-9
919 [29] H. Hashim et al, "Investigation of Annealing Temperature on Copper Oxide Thin Films
920 Using Sol-Gel Spin Coating Technique", *IOP Conference Series Materials Science and
921 Engineering*, 340(1), 012008, 2018, https://doi.org/10.1088/1757-899x/340/1/012008
922 [30] Tolansky, S., "Multiple Beam Interferometry of Surface and Films", Oxford University
923 Press, London, 1948.
924 [31] F. T. L. Muniz, M. A. R. Miranda, C. Morilla dos Santos and J. M. Sasaki, "The
925 Scherrer equation and the dynamical theory of X-ray diffraction", *Acta Crystallographica
926 Section A*, 2016, A 72, 385-390, doi.org/10.1107/S205327331600365X
927 [32] Sharma, R. K., Patel, S., & Pargaien, K. C. (2012). Synthesis, characterization and
928 properties of Mn-doped ZnO nanocrystals. Advances in Natural Sciences: Nanoscience and
929 Nanotechnology, 3(3), 035005.   http://doi:10.1088/2043-6262/3/3/035005

930 [33] Triloki, P. Garg, R. Rai, B. K. Singh, "Structural characterization of "as-deposited"
931 cesium iodide films studied by X-ray diffraction and transmission electron microscopy
932 techniques", *cond-mat. mtrl-sci*, 2013, arXiv:1211.5540v3
933 [34] Alessio Becheri, Maximilian Dürr, Pierandrea Lo Nostro, Piero Baglioni, "Synthesis and
934 characterization of zinc oxide nanoparticles: application to textiles as UV-absorbers", 2008,
935 10, 679–689, https://link.springer.com/article/10.1007/s11051-007-9318-3
936 [35] S. Muthukumaran, R. Gopalakrishnan, "Structural, FTIR and photoluminescence studies
937 of Cu doped ZnO nanopowders by co-precipitation method", *Opt. Mater.*, 2012, 34, 1946–
938 1953.doi.org/10.1016/j.optmat.2012.06.004
939 [36] Xiong, G., Luo, L., Li, C., & Yang, X. (2009). "Synthesis of Mesoporous ZnO (m-ZnO)
940 and Catalytic Performance of the Pd/m-ZnO Catalyst for Methanol Steam Reforming".
941 *Energy & Fuels*, 23(3), 1342–1346.
942 http://doi:10.1021/ef8008376
943 [37] Hussein, M. Z., Al Ali, S. H., Zainal, Z., & Hakim, M. N. (2011). Development of
944 antiproliferative nanohybrid compound with controlled release property using ellagic acid as
945 the active agent. International Journal of Nanomedicine, 6(1), 1373–1383.
946 http://doi:10.2147/IJN.S21567
947 [38] Xiong, G., Luo, L., Li, C., & Yang, X. (2009). "Synthesis of Mesoporous ZnO (m-ZnO)
948 and Catalytic Performance of the Pd/m-ZnO Catalyst for Methanol Steam Reforming".
949 *Energy & Fuels*, 23(3), 1342–1346.
950 http://doi:10.1021/ef8008376
951 [39] P. Dhamodharan, R. Gobi, N. Shanmugam, N. Kannadasan, R. Poonguzhali, S. Ramya,
952 "Synthesis and characterization of surfactants assisted Cu^{2+} doped ZnO nanocrystals",
953 *Spectrochimica Acta Part A: Molecular and Biomolecular* Spectroscopy, 2014, 131, 125–
954 131, doi.org/10.1016/j.saa.2014.04.083.
955 [40] A. Modwi, M. A. Abbo, E. A. Hassan, Ammar Houas, "Adsorption kinetic and
956 photocatalytic degradation of malachite green (MG) via Cu/ZnO nanocomposites", *Journal*
957 *of Environmental Chemical Engineering*, 2017, 5, 5954–5960,
958 doi.org/10.1016/j.jece.2017.11.024
959 [41] P. Jongnavakit, P. Amornpitoksuk, S. Suwanboon, N. Ndiege, "Preparation and
960 photocatalytic activity of Cu-doped ZnO thin films prepared by the sol–gel method", *Appl.*
961 *Surf. Sci.*, 2012, 258, 8192–8198, doi.org/10.1016/j.apsusc.2012.05.021
962 [42] Ghiloufi, I., Ghoul, J. El, Modwi, A., & Mir, L. El. (2016). "Ga-doped ZnO for
963 adsorption of heavy metals from aqueous solution". *Materials Science in Semiconductor*
964 *Processing*, 42(3), 102–106. http://doi:10.1016/j.mssp.2015.08.047
965 [43] Oskoei, V., Dehghani, M. H., Nazmara, S., Heibati, B., Asif, M., Tyagi, I., Gupta, V. K.
966 (2015). "Removal of humic acid from aqueous solution using UV/ZnO nano-photocatalysis
967 and adsorption". *Journal of Molecular Liquids*, 213, 374–380.
968 http://doi:10.1016/j.molliq.2015.07.052
969 [44] A. Ayeshamariam *et al*, "Synthesis and characterization of ZnO–CuO nanocomposites
970 powder by modified perfume spray pyrolysis method and its antimicrobial investigation",
971 *Journal of Semiconductors* 39 (3), 033001, 2018; http://doi:10.1088/1674-4926/39/3/033001
972 [45] K. Kaviyarasu et al, "Synthesis and characterization studies of MgO: CuO nanocrystals
973 by wet-chemical method", *Spectrochimica Acta Part A: Molecular and Biomolecular*
974 *Spectroscopy* 142, 405-409, 2015; https://doi.org/10.1016/j.saa.2015.01.111
975 [46] Y. Subba Reddy et al, "Equilibrium and kinetic studies of the adsorption of acid blue 9
976 and Safranin O from aqueous solutions by MgO decked FLG coated Fuller's earth", *Journal*
977 *of Physics and Chemistry of Solids 123,*
978 *43-51, 2018*; https://doi.org/10.1016/j.jpcs.2018.07.009

979 [47] Lee, H. J., Kim, B. S., Cho, C. R., and Jeong, S. Y., "A Study of Magnetic and Optical
980 Properties of Cu doped ZnO", *Phys. Stat. Sol.*, Vol-241, No. 7, pp 1533-1536,
981 2004.https://doi.org/10.1002/pssb.200304614
982 [48] Jongnavakit, P., Amornpitoksuk, P., Suwanboon, S., & Ndiege, N. (2012). "Preparation
983 and photocatalytic activity of Cu-doped ZnO thin films prepared by the sol–gel method".
984 *Applied Surface Science*, 258(20), 8192–8198. https://doi:10.1016/j.apsusc.2012.05.021
985 [49] Chauhan, Kumar A., and Chaudhary R. P., "Structure and Optical Properties of Zn $_{1-X}$ Ni
986 $_X$ O Nanoparticles by Coprecipitation Methodruby" *Journal of Optoelectronics and*
987 *Biomedical Materials* Vol. 3, Issue 1, P. 17-23, 2011.https://10.1007/s11164-011-0478-5
988 [50] Furdyna, J. K., "Diluted Magnetic Semiconductors", *Appl. Phys.*, Vol-64, No. 4,
989 1988.https://10.1063/1.341700
990 [51] Y. Zhang, B. Lin, Z. Fu, C. Liu, W. Han, "Strong ultraviolet emission and rectifying
991 behavior
992 of nanocrystalline ZnO films", *Opt. Mater.* 28,1192–1196 (2006);
993 https://doi:10.1016/j.optmat.2005.08.016
994 [52] V. Gandhi, R. Ganesan, H. Hameed, A. Syedahamed, M. Thaiyan, J. Phys. Chem. C
995 118, 9715–9725 (2014)
996 [53] Li, P., Wang, S., Li, J., & Wei, Y. (2012). "Structural and optical properties of Co-
997 doped ZnO nanocrystallites prepared by a one-step solution route". *Journal of*
998 *Luminescence*, 132(1), 220–225. http://doi:10.1016/j.jlumin.2011.08.019
999 [54] Xu, D. H., & Shen, W. Z. (2012). Cu-doped ZnO hemispherical shell structures:
1000 Synthesis and room-temperature ferromagnetism properties. *Journal of Physical Chemistry*
1001 *C*, 116(24), 13368–13373. http://doi:10.1021/jp3003849
1002 [55] Udayabhaskar, R., Mangalaraja, R. V, & Karthikeyan, B. (2013). "Thermal annealing
1003 induced structural and optical properties of Ca doped ZnO nanoparticles". *Journal of*
1004 *Materials Science: Materials in Electronics*, 1–6.
1005 http://doi:10.1007/s10854-013-1225-z
1006 [56] A O Zotov et al, "Electrical conductivity of Cu/ZnO/Si heterostructures", *IOP Conf.*
1007 *Series: Journal of Physics*: Conf. Series 816 (2017) 012013; https://10.1088/1742-
1008 6596/816/1/012013.
1009